TECTONICS, VOL. 28, TC4007, doi:10.1029/2008TC002403, 2009

Click Here for Full Article

Late Cenozoic structural and tectonic development of the western margin of the central Andean Plateau in southwest Peru

Taylor F. Schildgen,[1,2] Kip V. Hodges,[3] Kelin X. Whipple,[3] Malcolm S. Pringle,[1] Matthijs van Soest,[3] and Katrina Cornell[1]

Received 6 October 2008; revised 4 March 2009; accepted 13 April 2009; published 18 July 2009.

[1] Structural and thermochronologic studies of the western margin of the central Andean Plateau show changing styles of deformation through time that give insights into tectonic evolution. In southwest Peru, uplift of the plateau proceeded in several distinct phases. First, NW striking, NE dipping reverse faults accommodated uplift prior to ~14–16 Ma. Subsequent uplift of the plateau relative to the piedmont (between the plateau and the Pacific Ocean) occurred between ~14 and 2.2 Ma and was accommodated by NW striking, SW dipping normal faults and subparallel monoclinal folds. The youngest phase of uplift affected the piedmont region and the plateau margin as a coherent block. Although the uplift magnitude associated with phase 1 is unknown, phases 2 and 3 resulted in at least 2.4–3.0 km of uplift. Up to 1 km of this may have occurred during phase 3. Geodynamic processes occurring in both the continental interior and the subduction zone likely contributed to uplift.

Citation: Schildgen, T. F., K. V. Hodges, K. X. Whipple, M. S. Pringle, M. van Soest, and K. Cornell (2009), Late Cenozoic structural and tectonic development of the western margin of the central Andean Plateau in southwest Peru, *Tectonics*, *28*, TC4007, doi:10.1029/2008TC002403.

1. Introduction

[2] The central Andean Plateau is the second largest topographic plateau on Earth, with average elevations of 4000 m extending over a region 300 km wide and ~1500 km long. While many geodynamic models have been proposed to explain the origin of great continental plateaus like the central Andean Plateau and Tibet, an often-neglected aspect of the debate is that the structural history of plateau margins provides an important constraint on the tectonic processes by which plateaus grow. Our focus in this paper is the western margin of the central Andean Plateau, where published accounts of the structure of the plateau margin, a topographic feature known as the Western Andean Escarpment (WAE), are inconsistent. The simple morphology of the WAE led several early researchers to suggest it developed as a result of simple flexure or tilting into a crustal-scale monocline [e.g., *Muñoz*, 1956; *Mortimer*, 1973; *Isacks*, 1988]. *Wörner et al.* [2002] supported this interpretation, noting over-steepened sedimentary deposits along the flanks of the margin in northern Chile. In contrast, several studies in northern Chile have suggested that the margin evolved over a high-angle, west vergent reverse fault system [e.g., *Muñoz and Charrier*, 1996; *García*, 2002; *Pinto et al.*, 2004; *Victor et al.*, 2004; *Farías et al.*, 2005]. The finding that most of this shortening ended prior to 10 Ma in northern and central Chile [e.g., *Victor et al.*, 2004; *Farías et al.*, 2005] implies that it cannot explain the significant post 10 Ma river incision of the western margin of southwest Peru and northern Chile [e.g., *Schildgen et al.*, 2007, 2008; *Thouret et al.*, 2007; *Hoke et al.*, 2007], and uplift of the central Andes more broadly (Table 1). On the basis of detailed mapping of some of the more accessible parts of the WAE in southwest Peru, this paper aims to evaluate the relative significance of reverse faulting, normal faulting, and monoclinal deformation in accommodating differential uplift across this segment of the WAE. We also explore the role these structures have played in uplift of the Western Cordillera and central Andean Plateau relative to sea level, and the distribution of that uplift in space and through time.

2. Geologic Setting of the WAE in Southern Peru–Northern Chile

[3] The subduction zone along the western margin of South America has been active since at least Cretaceous time, with periods of tectonism throughout the margin's history correlating broadly with variations in the subduction rate of the Nazca plate beneath the South American plate [e.g., *Pardo-Casas and Molnar*, 1987; *Somoza*, 1998], and subduction angle [*Jordan et al.*, 1983]. Southern Peru lies at the northern end of the Central Volcanic Zone, which is located above a relatively steeply dipping (~30°) section of the subducting slab. North of approximately 15.5°S latitude, the subduction zone transitions to a magmatically quiescent "flat slab" region with a subduction angle of ~15° [*Cahill and Isacks*, 1992; *Jordan et al.*, 1983].

[4] Between the trench and the WAE that defines the margin of the central Andean Plateau lies a broad fore-arc domain, which we refer to as the "piedmont" region. Most surface exposures in this region consist of clastic, predominantly continental rocks interstratified with ignimbrite

[1]Department of Earth, Atmospheric and Planetary Sciences, Massachusetts Institute of Technology, Cambridge, Massachusetts, USA.
[2]Now at Department of Geosciences, University of Potsdam, Potsdam, Germany.
[3]School of Earth and Space Exploration, Arizona State University, Tempe, Arizona, USA.

Copyright 2009 by the American Geophysical Union.
0278-7407/09/2008TC002403$12.00

Table 1. Constraints on Late Cenozoic Uplift for the Central Andes

Location	Uplift Magnitude (m)	Initiation (Ma)	Method/Evidence	Reference
Corocoro, Altiplano	2000 ± 2000	10–15	paleobotany	*Singewald and Berry* [1922]
Potosi, Altiplano	3040 ± 1260	13.8–20.8	paleobotany	*Gregory-Wodzicki* [2000]
Jakokkota, Altiplano	2535 ± 1405	10–11	paleobotany	*Gregory-Wodzicki* [2000]
Callapa, Altiplano	2500–3500	10.3	oxygen isotopes	*Garzione et al.* [2006]
Callapa, Altiplano	3400 ± 600	10.3	clumped isotopes	*Ghosh et al.* [2006]
Callapa, Altiplano	2500 ± 1000	10.3	clumped isotopes	*Quade et al.* [2007]
N. Chile, W. Cordillera	>1400	10	rotated basin fill	*Nester et al.* [2006]
N. Chile, W. Cordillera	250–1800	10	rotated lake beds	*Jordan et al.* [2006]
N. Chile, W. Cordillera	~1000	10	incised paleosurfaces	*Hoke and Garzione* [2008]
N. Chile, W. Cordillera	1000–2000	10	incised paleosurfaces	Garzione and Hoke (2006)[a]
S. Peru, W. Cordillera	>2400	10	incised canyons	*Schildgen et al.* [2007]
S. Peru, W. Cordillera	2000–2500	13–9	incised canyons	*Thouret et al.* [2007]
N. Chile, W. Cordillera	>1000	~10	incised canyons	*Hoke et al.* [2007]
N. Chile/S. Bolivia	variable	~10	uplifted paleosurfaces	*Hoke and Garzione* [2008]
Potosi, E. Cordillera	1500 ± 2000	13.8–20.8	paleobotany	*Berry* [1939]
Bolivia, E. Cordillera	1950 ± 1250	12–9	incised paleodrainages	*Kennan et al.* [1997]
Pislepampa, E. Cordillera	2300 ± 1100	6–7	paleobotany	*Graham et al.* [2001]
Bolivia, E. Cordillera	1705 ± 695	12–9	incised paleodrainages	*Barke and Lamb* [2006]

[a]C. N. Garzione and G. D. Hoke, Paleoelevation and geomorphic constraints on the late Miocene rise of the Andes: Geodynamic implications for the growth of orogenic plateaus, paper presented at 16th V.M. Goldschmidt Conference, Melbourne, Victoria, Australia, 2006.

sheets that provide valuable time markers. Unfortunately, the stratigraphic nomenclature for these units is inconsistent in published literature. We will generally follow the most recently published chronostratigraphy of *Thouret et al.* [2007]. Of specific interest to us are the Tertiary units in the piedmont region that predate incision of the great canyons that drain the central Andean Plateau. These units will be referred to simply as the Moquegua group. Clastic rocks in the Moquegua group were shed from the evolving Andes to the north and east. Deposition of the Moquegua group began sometime before 30 Ma and perhaps as early as 50 Ma [*Roperch et al.*, 2006; T. Sempere et al., Estratigrafía, geochronología, paleogeografía y paleotectónica de los dépositos de antearco del sur del Perú, paper presented at XII Congreso Peruano de Geología, Sociedad Geológica del Perú, Lima, 2004]. Early deposition, which we refer to as the "lower Moquegua group," was dominated by siltstones and sandstones that are preserved today as red beds. An unconformity at ~30 Ma (Sempere et al., presented paper, 2004) marks a transition to coarser sandstones and gravels, which we refer to as the "upper Moquegua group." Beginning about 24.5 Ma, the upper Moquegua stratigraphy was punctuated by episodic ignimbrite flows. The number and thickness of these flows increase upward in the section. The top of the Moquegua group corresponds to a thick set of ignimbrite sheets dated at between 14.3 and 13.2 Ma by *Thouret et al.* [2007]. Collectively, the 16.1–13.2 Ma ignimbrites form a regionally extensive caprock, and the dip of this caprock largely defines the topographic slope of the piedmont region, Additional, younger gravels (referred to as the "Moquegua D" unit by some workers (e.g., Sempere et al., presented paper, 2004)) form terraces and pediments that postdate deformation on all faults mapped in the region and often form cut-and-fill channel sequences. Although the age range of these gravels is unknown, a 4.95 ± 0.03 Ma ash layer (sample 07TS16 (Figure 1 and Tables 2 and 3)) ~10 m below the top of the section in the Vitor valley and zircon (U-Th)/He ages of 6.70 ± 0.31 Ma, 6.79 ± 0.16 Ma, and 6.96 ± 0.18 Ma from another intercalated ash layer ~50 m beneath the top in the Sihuas valley (sample 07TS15 (Figure 1 and Table 4)) suggest a late Miocene to Pliocene age. These Mio-Pliocene gravels form a regional "bajada" surface that is prominent throughout the fore-arc region (Figure 1). The upper few meters of the Mio-Pliocene bajada has been reworked to varying degrees during the Quaternary and is consequently often mapped as Quaternary, but the bajada essentially retains its Mio-Pliocene morphology.

[5] Unconformities within the Moquegua group, such as the one between the upper and lower groups, record the early deformational history of the southwestern Peruvian Andes. The earliest "Incaic" phase, likely responsible for the formation of highlands that were the source region of the lower Moquegua group, included high-angle, west vergent reverse faulting prior to 45–40 Ma [*Steinmann*, 1929; *Noble et al.*, 1979, 1990]. High-angle faults that cut strata of the upper Moquegua group are frequently ascribed to the early Miocene "Quechua" phase of deformation [*Mégard*, 1984]. However, these structures in many places also cut the 16.1–13.2 Ma ignimbrites and thus also record post–Middle Miocene deformation [*Schildgen et al.*, 2007; *Thouret et al.*, 2007]. M. Sébrier et al. (Evolución neogena del piedemonte Pacifico de los Andes del sur del Perú, paper presented at Segundo Congreso Geológico Chileno, Sociedad Geológica de Chile, Arica, Chile, 1979) and *Tosdal et al.* [1984] also inferred a significant amount of post–Middle Miocene from geologic relationships observed in southwest Peru.

[6] In southwest Peru, the topographic character of the WAE changes significantly along strike. In the eastern part of our study area, east of the Colca-Majes valley (Figure 1), the escarpment marks a steep 2-km range front. Topographic swath profiles from the region show that the piedmont region has an average slope of 1.1°, within the range of expected depositional slopes of the sediments covering the

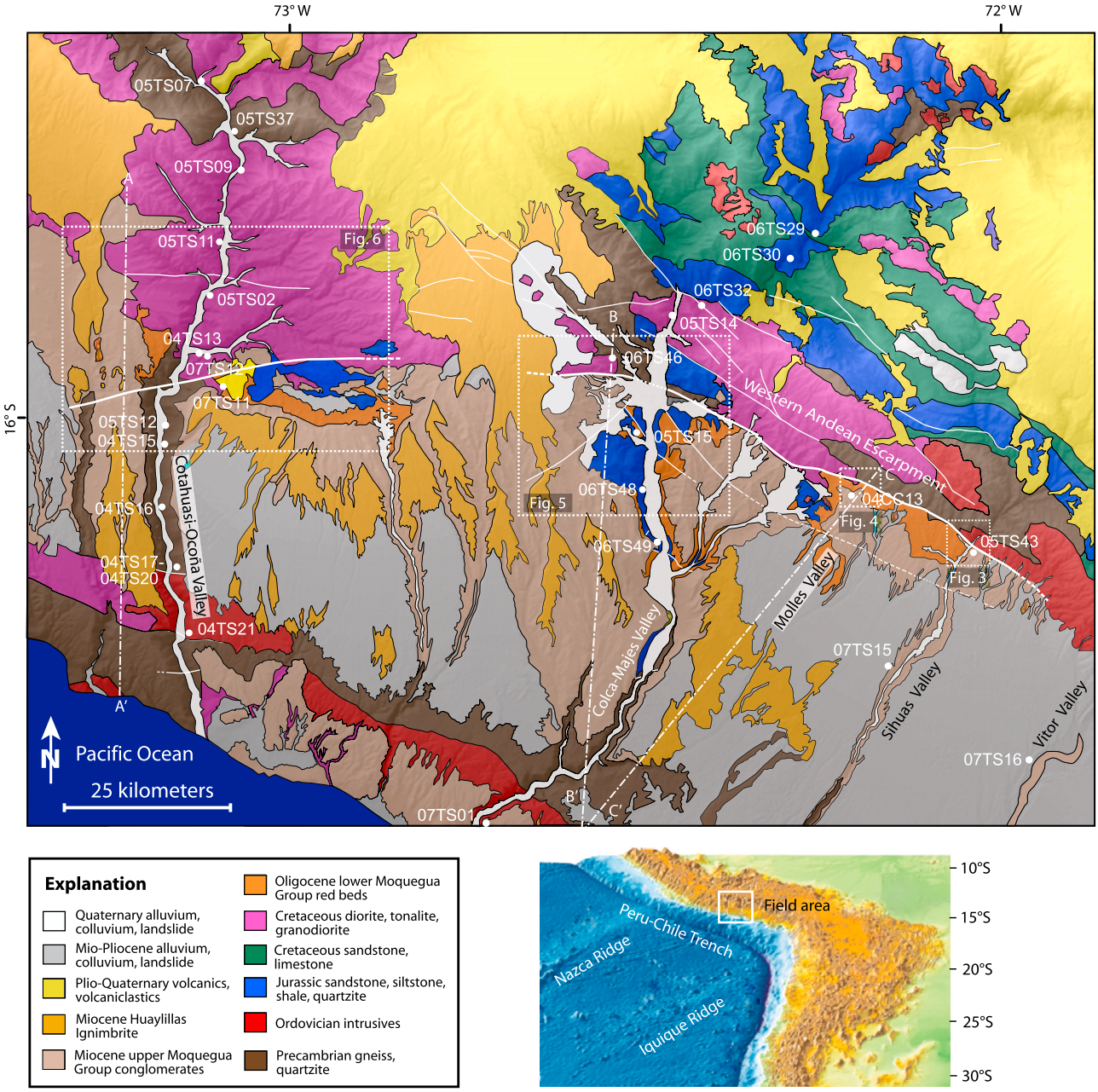

Figure 1. Location map showing simplified geology and regional morphology of southern Peru. Geology layer is draped over both a semitransparent 30-m resolution digital elevation model derived from Advanced Spaceborne Thermal Emission and Reflection Radiometer (ASTER) imagery and a shaded relief map. Faults are shown as white lines. Inferred faults are shown as dashed white lines, and buried faults are shown as dotted white lines. Dotted rectangles show regions of focused structural mapping. White dots show sample locations. Dash-dotted white lines show locations of geological cross sections. Perspective view of central Andes topography and bathymetry is based on GTOPO30 bathymetry data and SRTM onshore topographic data.

area (as determined using the method of *Paola and Mohrig* [1996]). Slopes steepen abruptly to 6.0° across the escarpment, then decrease again at high plateau elevations. West of the Colca-Majes valley, the escarpment morphology transitions to a gentle ramp, characterized by a gradual increase in elevation (Figure 2), and only a slight steepening at the range front. The changing geometry of this ramp is defined especially well by a sequence of 16.1–13.2 Ma ignimbrite flows that form the caprock of the regional topographic surface. Near the Cotahuasi-Ocoña valley, the

Table 2. Description and Context for $^{40}Ar/^{39}Ar$ Samples[a]

Sample	Description	Latitude	Longitude	Age ± 2σ (Ma)
05TS43	Undeformed ignimbrite crossing range front fault zone near Lluclla	16°11′16.08″	72°01′36.33″	16.12 ± 0.04
04TS10	Huaylillas Ignimbrite near Toro Muerto (south of Aplao)	16°14′45.83″	72°30′06.56″	14.20 ± 0.04
04TS22	Huaylillas Ignimbrite near range front north of Aplao	15°57′20.85″	72°34′59.70″	14.29 ± 0.04
04CC13	Warped ash unit within Moquegua formation south of range front north of Pedregal	16°06′42.93″	72°12′18.51″	14.11 ± 0.05
04CC12	Undeformed basaltic andesite crossing range front fault zone north of Pedregal	16°05′45.72″	72°11′47.54″	0.21 ± 0.04
07TS12	Tuff perched 200 m above valley floor in Iquipi Valley	15°55′40.012″	73°04′21.390″	2.01 ± 0.03
07TS11	Tuff blanketing low bench in Iquipi side valley (north side Iquipi fault)	15°59′04.518″	73°04′49.050″	2.06 ± 0.05
07TS16	Tuff in coarse, loose gravels in Vitor Valley above Moquegua formation	16°27′27.726″	71°57′15.738″	4.95 ± 0.03
07TS13	Tuff in tilted beds north side of thrust in Majes Valley	16°21′23.586″	72°27′51.384″	16.26 ± 0.08
07TS08	Tuff in Cuno-Cuno section of Moquegua formation, near Iquipi	15°59′56.016″	73°05′08.700″	23.80 ± 0.16
PIG-03-126	Ignimbrite capping Cuno-Cuno section of Moquegua formation near Iquipi	16°00′31.221″	73°05′16.508″	13.19 ± 0.07

[a]Latitude and longitude are south and west, respectively.

regional slope of 2.2° between the coastal escarpment and the plateau is twice as steep as the alluvial plain in the piedmont region east of the Colca-Majes valley. In this location, there is no clear distinction between the piedmont and the WAE; the WAE effectively extends to the coast. A swath profile parallel to the coast showcases the along-strike variation; piedmont elevations near the Ocoña valley are c. 700 m higher than at equivalent distance from the coast near the Majes valley. This dramatic change in WAE and piedmont morphology motivated our regional tectonic study. Are the differing morphologies an indication of different structural styles, or could the low slopes to the west simply indicate that the fault system marking the WAE to the east has been obscured by flanking sediments and the overlying 16.1–13.2 Ma ignimbrites? Were the latter interpretation correct, it would provide a minimum age constraint on the age of WAE formation. In the following sections, we describe four transects across the WAE. Geologic mapping, structural observations, bedrock thermochronology, and volcanic geochronology of these areas provide a rich history of the evolution of the WAE in southwestern Peru.

3. Study Areas

[7] Our four study transects correspond to areas where the WAE is cut by rivers draining nearby highlands of the western Cordillera (Figure 1). From southeast to northwest, they are the Sihuas valley, the Molles valley, the Colca-Majes valley, and the Cotahuasi-Ocoña valley. In addition to this, reconnaissance studies of the coastal escarpment provided context for understanding coupled uplift of the piedmont and plateau region relative to sea level.

[8] Base maps we used in mapping included 1:100,000-scale topographic maps generated by the Instituto Geografico Militar Lima, Peru, 15-m resolution Advanced Spaceborne Thermal Emission and Reflection Radiometer (ASTER) satellite imagery, and shaded relief maps generated from 30-m resolution ASTER-derived digital elevation data. This

Table 3. Age Spectra Analysis for $^{40}Ar/^{39}Ar$ Data[a]

			Age Spectra				Isochron Analysis			
Sample	Material	K/Ca	Percent Gas	N[b]	MSWD	Weighted Age (Ma)	Age (Ma)	$^{40}Ar/^{36}Ar$ Intercept	MSWD	Reference[c]
05TS43	Sanidine	59.3	100	20 of 20	0.82	16.12 ± 0.04	16.1 ± 0.05	272 ± 68	0.85	1
04TS10	Sanidine	70.8	100	12 of 12	1.29	14.20 ± 0.04	14.2 ± 0.04	291 ± 9	1.28	1
04TS10	Biotite	12.1	95.9	9 of 18	1.68	14.32 ± 0.05	14.3 ± 0.20	296 ± 20	1.93	this paper
04TS22	Sanidine	50.2	100	11 of 11	2.00	14.29 ± 0.04	14.30 ± 0.05	294 ± 47	2.21	1
04TS22	Biotite	10.8	90.7	9 of 19	1.46	14.35 ± 0.05	14.31 ± 0.21	300 ± 19	1.62	this paper
04CC13	Sanidine	84.1	100	10 of 10	0.73	14.11 ± 0.05	14.1 ± 0.14	330 ± 236	0.72	this paper
04CC13	Biotite	9.68	100	10 of 10	0.66	14.39 ± 0.12	14.2 ± 0.8	323 ± 145	0.60	this paper
04CC12	Groundmass	0.38	68.6	6 of 14	2.13	0.21 ± 0.04	NA	NA	NA	this paper
07TS12	K-feldspar	1.99	92.8	17 of 20	0.59	2.01 ± 0.03	NA	NA	NA	this paper
07TS11	K-feldspar	0.64	100	18 of 18	0.83	2.06 ± 0.05	NA	NA	NA	this paper
07TS11	Biotite	9.47	100	5 of 5	1.18	2.07 ± 0.03	NA	NA	NA	this paper
07TS16	Sanidine	45.4	100	19 of 19	2.65	4.95 ± 0.03	NA	NA	NA	this paper
07TS13	Sanidine	71.1	100	10 of 10	2.29	16.26 ± 0.08	NA	NA	NA	this paper
07TS13	Biotite	13.0	100	12 of 12	0.28	17.01 ± 0.42	NA	NA	NA	this paper
07TS08	K-Feldspar	0.38	100	18 of 18	0.8	23.80 ± 0.16	NA	NA	NA	this paper
07TS08	Biotite	9.2	91.9	11 of 12	0.75	24.11 ± 0.11	NA	NA	NA	this paper
PIG-03-126	Feldspar	NA	NA	NA	NA	13.21 ± 0.53	NA	NA	NA	2
PIG-03-126	Biotite	NA	NA	NA	NA	13.19 ± 0.07	NA	NA	NA	2

[a]NA, not available.
[b]Refers to number of steps on age plateau out of total number of steps or number of grains analyzed for single-grain analyses.
[c]References are 1, *Schildgen et al.* [2007]; 2, *Thouret et al.* [2007].

Table 4. Zircon and Apatite (U-Th)/He Data[a]

Sample	Th/U	Mass (μg)	Radius (μg)	U (ppm)	Th (ppm)	^{4}He (nmol/g)	Ft/HAC	Age[b] (Ma)	2 σ[c] (Ma)	Distance[d] (km)	Elevation (m)	Reference[e]
						Ocoña Valley Zircons						
04TS12zA	0.72	5.25	43.5	269	188	101	0.77	77.4	2.8	5.4	702	1
04TS12zB	0.89	6.78	42.5	194	168	81.5	0.77	83.4	2.9	5.4	720	1
04TS13z_B	0.47	2.92	38.3	233	106	90.9	0.73	88.9	4.5	0.7	552	1
04TS13z_A	0.63	3.31	37.5	277	169	125	0.73	99.0	5.0	0.7	552	1
04TS15zA	0.27	2.65	40.8	408	108	201	0.75	115	4.4	−14.3	322	1
04TS15zB	0.32	1.98	40.5	361	111	151	0.73	98.4	3.8	−14.3	322	1
04TS16z_A	2.79	14.7	59.8	94.5	257	110	0.82	158	7.3	−23.3	225	1
04TS16z_B	0.55	14.7	65.3	170	91.4	134	0.84	153	7.7	−23.3	225	1
04TS18z_A	2.78	7.80	56.8	56.5	153	74.3	0.81	182	8.3	−23.3	415	1
04TS18z_B	1.31	6.82	57.3	122	156	121	0.81	173	8.2	−23.3	415	1
04TS20z_A	1.16	2.22	37.5	200	227	210	0.72	210	9.9	−31.0	650	1
04TS20z_B	1.46	4.14	51.5	123	174	123	0.78	177	8.1	−31.0	650	1
04TS21zA	0.82	14.6	52.5	78.8	62.7	57.3	0.82	138	4.9	−38.6	73	1
04TS21zB	1.26	6.96	48.3	61.7	75.6	52.3	0.78	155	5.3	−38.6	73	1
05TS02z_A	0.83	14.5	54.7	206	166	87.3	0.82	79.9	3.8	10.1	590	1
05TS02z_B	0.48	8.21	50.4	340	160	143	0.80	87.5	4.3	10.1	590	1
05TS07z_A	0.52	13.3	55.3	228	115	53.0	0.82	46.7	2.3	39.2	939	1
05TS07z_B	0.43	12.5	54.3	195	80.8	40.7	0.82	43.1	2.1	39.2	939	1
05TS09z_A	0.63	12.4	63.9	365	223	116	0.83	61.7	3.0	29.1	816	1
05TS09z_B	1.41	10.3	56.2	600	823	319	0.81	91.2	4.2	29.1	816	1
05TS11z_A	0.46	43.8	80.4	294	132	110	0.88	71.2	3.5	17.7	647	1
05TS11z_B	0.58	52.8	93.0	202	114	80.2	0.89	72.8	3.5	17.7	647	1
05TS12z_A	1.14	20.8	67.0	57.7	64.3	36.7	0.85	110	4.8	−11.0	360	1
05TS12z_B	0.66	17.7	59.7	111	71.3	71.3	0.84	123	5.6	−11.0	360	1
05TS37z_A	0.337	14.0	60.7	162	54.6	30.4	0.83	38.6	2.0	33.5	850	1
05TS37z_B	0.425	14.1	58.2	117	49.8	25.3	0.83	43.8	2.3	33.5	850	1
						Majes Valley Zircons						
05TS14z-A	0.85	3.20	32.2	932	768	204	0.71	72.5	1.9	12.0	848	2
05TS14z-B	0.78	3.15	36.1	1274	962	274	0.73	71.3	1.8	12.0	848	2
05TS15z-A	**0.31**	**7.46**	**54.3**	**248**	**76**	**120**	**0.80**	**103**	**32.1**	**−7.3**	**736**	**2**
05TS15z-B	0.82	7.67	53.1	488	389	200	0.80	79.0	2.0	−7.3	736	2
05TS15z-C	0.82	7.00	57.1	178	106	67	0.80	75.4	2.3	−7.3	736	2
05TS15z-D	0.61	8.01	57.8	410	402	148	0.81	66.8	1.9	−7.3	736	2
05TS15z-E	1.01	4.02	38.6	417	252	150	0.75	77.2	2.1	−7.3	736	2
06TS29z-A	0.87	2.16	31.7	298	251	136	0.69	101	3.1	32.8	1300	2
06TS29z-B	0.32	2.15	32.9	322	101	244	0.70	184	5.5	32.8	1300	2
06TS29z-C	0.25	2.15	33.5	236	57	7	0.70	7.8	0.22	32.8	1300	2
06TS29z-D	0.37	2.04	33.9	197	72	133	0.70	163	4.4	32.8	1300	2
06TS29z-E	0.59	2.76	31.7	247	143	10	0.70	9.2	0.23	32.8	1300	2
06TS30z-A	0.49	2.63	33.5	180	85	56.5	0.71	73.1	2.3	28.5	1177	2
06TS30z-B	1.38	3.07	41.5	89	119	31.8	0.74	68.1	2.0	28.5	1177	2
06TS30z-D	0.68	4.28	34.5	54	36	12.5	0.73	50.0	1.7	28.5	1177	2
06TS30z-E	0.22	4.56	42.9	317	69	142.9	0.76	103	3.1	28.5	1177	2
06TS32z-A	**2.21**	**4.60**	**42.0**	**541**	**1167**	**139**	**0.75**	**41.8**	**21**	**15.4**	**1000**	**2**
06TS32z-B	0.94	4.54	43.7	422	387	162	0.75	77.0	2.0	15.4	1000	2
06TS32z-C	0.53	9.45	48.7	342	178	111	0.80	66.2	1.9	15.4	1000	2
06TS32z-D	0.62	10.7	49.9	328	198	114	0.81	69.2	1.9	15.4	1000	2
06TS32z-E	0.66	10.3	60.0	146	93	43	0.82	58.0	1.7	15.4	1000	2
06TS46z-A	0.76	26.4	70.9	244	182	87	0.86	65.2	1.9	1.3	1293	2
06TS46z-B	0.62	23.2	74.0	392	237	123	0.86	58.8	1.7	1.3	1293	2
06TS47z-A	0.35	12.1	53.6	324	112	70	0.82	44.8	1.2	14.0	1090	2
06TS47z-B	0.57	5.77	45.3	292	163	90	0.78	64.7	1.7	14.0	1090	2
06TS47z-C	0.57	30.3	83.5	207	115	68	0.87	60.9	1.8	14.0	1090	2
06TS47z-D	0.56	20.4	79.2	245	135	83	0.76	63.9	1.9	14.0	1090	2
06TS47z-E	0.52	5.72	42.2	512	259	116	0.77	48.5	1.3	14.0	1090	2
06TS49z-A	**0.85**	**6.26**	**49.3**	**102**	**84**	**42.3**	**0.79**	**81.4**	**3.0**	**−17.6**	**490**	**2**
06TS49z-B	0.39	5.07	45.7	329	129	153	0.77	101	3.2	−17.6	490	2
06TS49z-C	0.69	22.28	72.2	150	101	117	0.86	143	3.8	−17.6	490	2
06TS49z-D	0.27	11.24	60.6	458	118	264	0.82	121	3.6	−17.6	490	2
06TS49z-E	0.46	18.62	71.6	210	95	151	0.85	140	4.2	−17.6	490	2

Table 4. (continued)

Sample	Th/U	Mass (μg)	Radius (μg)	U (ppm)	Th (ppm)	^{4}He (nmol/g)	Ft/HAC	Age[b] (Ma)	2 σ[c] (Ma)	Distance[d] (km)	Elevation (m)	Reference[e]
Majes Valley Apatites												
05TS14-A	2.27	4.04	52.0	13	29	0.85	0.74	10.6	0.45	12.0	848	2
05TS14-B	2.09	2.35	46.1	12	26	0.54	0.70	7.70	0.38	12.0	848	2
05TS14-C	2.68	5.73	53.6	11	29	0.81	0.75	11.2	0.46	12.0	848	2
05TS14-D	1.98	2.64	49.9	12	25	0.88	0.72	12.2	0.55	12.0	848	2
05TS15-A	3.13	1.94	43.0	22	68	1.34	0.68	9.60	0.41	−7.3	736	2
05TS15-B	3.09	1.72	41.7	19	58	1.18	0.67	10.1	0.43	−7.3	736	2
Camana Zircons From Reworked Ash												
07TS01-A	1.08	9.59	40.3	441	464	73.2	0.77	21.5	0.52	n/a	370	2
07TS01-B	1.52	3.74	31.2	131	194	310	0.71	305	8.7	n/a	370	2
07TS01-C	0.82	4.61	47.1	162	129	300	0.77	250	6.3	n/a	370	2
07TS01-D	0.68	2.12	31.1	228	152	28.5	0.69	19.6	0.46	n/a	370	2
07TS01-E	1.32	2.83	34.9	67	86	108	0.71	213	5.6	n/a	370	2
Sihuas Valley Zircons From Ash												
07TS15-A	0.73	5.27	43.6	356	255	17.4	0.77	6.79	0.16	n/a	1450	2
07TS15-B	0.53	5.73	44.5	928	479	44.9	0.77	6.96	0.17	n/a	1450	2
07TS15-C	2.02	4.08	45.9	95	187	72.3	0.75	86.1	2.1	n/a	1450	2
07TS15-D	2.95	3.50	38.4	2693	1810	84.3	0.73	8.23	0.38	n/a	1450	2
07TS15-E	2.90	4.50	31.4	380	347	65.5	0.76	6.70	0.31	n/a	1450	2

[a]Bold rows indicate grains with low ICP counts relative to background. These were not plotted in Figure 8.
[b]Ages corrected for alpha ejection.
[c]Error includes analytical precision only; in reality, zoning in U and Th also likely contribute to uncertainty.
[d]Distance measured from range front; negative direction is toward the coast, and positive is toward the arc.
[e]Here 1, *Schildgen et al.* [2007]; 2, this paper.

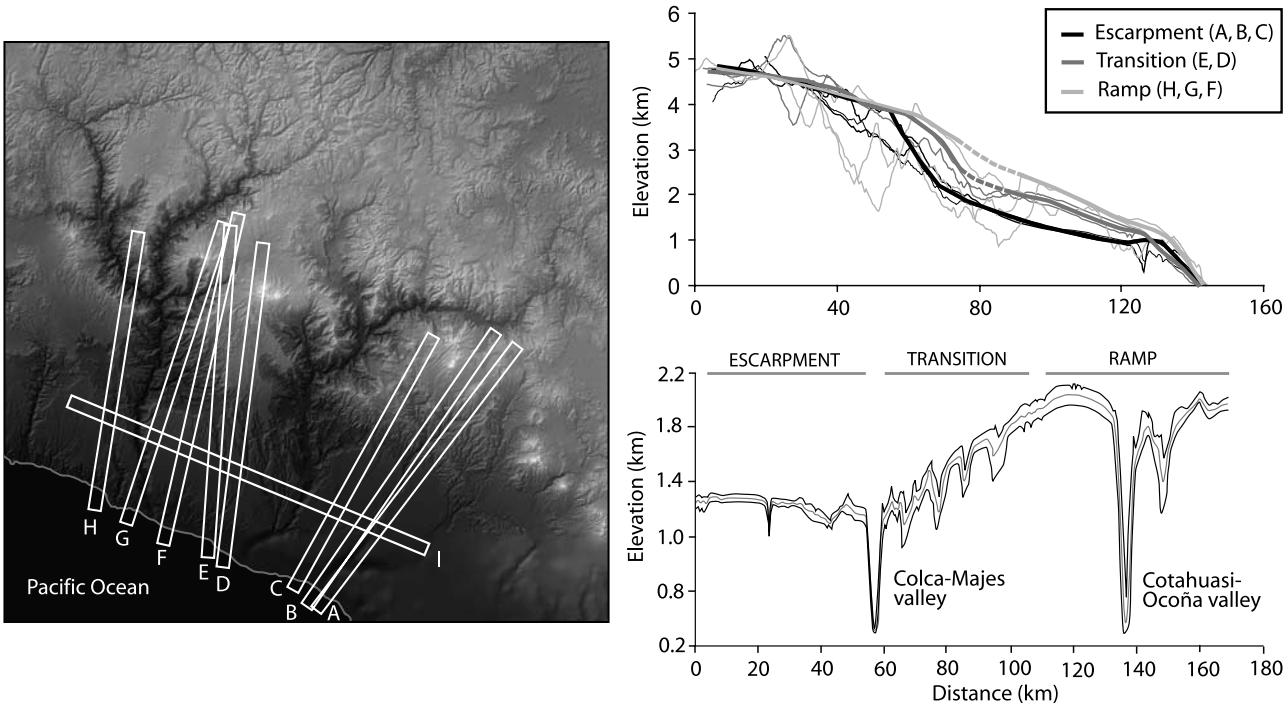

Figure 2. Topographic swath profiles derived from 90-m resolution Shuttle Radar Topography Mission (SRTM) digital elevation data. Swaths selected are 6 km wide and traverse the region starting from the escarpment morphology east of the Colca-Majes drainage and moving toward the ramp morphology of the Cotahuasi-Ocoña drainage. Thin gray lines show the mean elevations from each swath profile, and thick gray lines show simplified profiles created by projecting the regional surface across drainages. Dashed sections of thick gray lines show the inferred location of the eroded regional surface. Single swath profile oriented subparallel to coastline (box I), showing minimum, mean, and maximum elevations within the swath.

digital elevation model (DEM) was created by merging 32 individual ASTER-derived DEMs in ArcINFO to create a single high-resolution DEM covering the field area. Data dropouts, typically related to clouds in ASTER scenes, were filled with 90-m resolution Shuttle Radar Topography Mission (SRTM) digital elevation data. The two DEM data sets combined in this way rendered topography throughout the landscape with very few holes, which are typically common in SRTM data in steep and narrow canyons. Three-dimensional rendering of 15-m resolution ASTER imagery draped over the DEM provided a useful aid to mapping and morphological analysis. All structural observations and sample locations were georeferenced using ESRI *ArcPad* software running on Compaq-HP *iPAQ* handheld computers coupled with Bluetooth-enabled GPS receivers. Base maps, structural observations, and sample locations were compiled into a single project in ESRI *ArcMap*. Sample preparation methods and analytical protocols for $^{40}Ar/^{39}Ar$ and (U-Th)/He geochronology are described in Appendix A.

3.1. Sihuas Valley

[9] In the Sihuas valley (Figure 3), the WAE is marked by the Lluclla fault zone (the "Lluclla fault" of *Sébrier et al.* [1985]). In general, the fault zone separates Mesozoic intrusive igneous rocks to the northeast from Moquegua group rocks to the southwest. The zone itself is structurally complex, containing blocks of highly sheared igneous rocks and structurally disrupted panels of sedimentary rocks. The principal, throughgoing strand of the fault zone is a relatively low angle (30–40°), SW dipping normal fault that, while not well exposed, marks the local range front. A hanging wall splay from this fault is much better exposed (Figure 3b). Striking subparallel to the principal strand (~N35°W) but dipping more steeply, this fault intercalates decimeter-scale blocks from the footwall intrusive rocks with crushed Moquegua hanging wall sediments. Cataclastic shear fabrics are pervasive in the intrusive rocks. Although their orientations vary, the most pronounced shear surfaces strike subparallel to the range front escarpment and dip steeply southwestward or northeastward. Slickenlines are relatively rare on fault surfaces within the shear zone and have a wide variety of orientations. Deformation is more limited in the hanging wall Moquegua strata. Structures include a series of minor faults with offsets of one to several meters and monoclinal folds dipping up to 10°S with wavelengths of several tens to hundreds of meters. Disturbance of the Moquegua stratigraphy is greatest near the fault zone, where beds have been dragged into orientations dipping up to 35° away from the escarpment. The orientations of these folds, as well as the morphology of the escarpment, imply an important component of normal sense displacement. On the basis of stress inversions of fault and slickenline orientation data from the Lluclla fault zone, *Sébrier et al.* [1985] inferred NNE-SSW extensional kinematics for the youngest phase of faulting. The total amount of vertical throw on the fault zone is poorly constrained, but must be at least the 500–600-m height of the steep mountain front in this area since no units equivalent to the offset Moquegua strata occur in the footwall. What proportion of this offset occurred prior to deposition of the Moquegua sediments is presently unknown.

[10] *Sébrier et al.* [1985] argued that the Lluclla fault zone had a complex deformation history that included an old phase of contractile deformation prior to NNE-SSW extension. Evidence for this is not clear, but may be indicated by the shears of wide-ranging orientation within the footwall intrusive rocks (e.g., middle stereoplot in Figure 3a). None of this earlier deformation affects the Moquegua strata, but there is evidence for multiple phases of extension throughout the deformed fault zone. On the SE side of the valley, near the valley floor, exposures of the Moquegua group are dominated by red beds that are lithologically similar to those that characterize the lower Moquegua group in other regions of southwestern Peru. At higher elevations up the SE valley wall, these red beds pass upward into tan conglomerates that are characteristic of the upper Moquegua group across an angular unconformity. We tentatively correlate this unconformity with the lower-upper Moquegua unconformity elsewhere. At this location, the high-angle fault shown in Figure 3b cuts the Moquegua red beds but does not disturb supraunconformity Moquegua group gravels. A few tens of meters above the unconformity is an intercalated 16.12 ± 0.04 Ma ignimbrite (sample 05TS43 (Tables 2 and 3)), which limits most recent slip on the high-angle strand to before 16.12 Ma. However, the ignimbrite projects into the principal, low-angle strand of the fault zone, and that low-angle feature clearly cuts gravels roughly 20 m below the ignimbrite. This implies that the latest slip on the principal fault is younger than roughly 16.12 Ma.

3.2. Molles Valley

[11] Published 1:100,000-scale geologic maps of southwest Peru from the *Instituto Geológico Minero y Metalúrgico* (*INGEMMET*) [2001] suggest that early Andean deformational activity in the Molles valley (Figure 1) included development of a number of west to WNW striking reverse faults and associated fault propagation folds in pre-Tertiary lithologic units. The overlying Moquegua sediments exposed in valley walls generally show no deformation or only minor folding into monoclines that is likely related to late reactivation of these faults to accommodate differential vertical movements in the piedmont.

[12] Where the WAE crosses the Molles valley (Figure 4), the dramatic range front seen today can be attributed to structural uplift of pre-Tertiary igneous units of the Western Cordillera relative to Moquegua strata of the piedmont. On the basis of a shaded relief image created from the DEM and satellite imagery, the fault zone responsible for this can be correlated with confidence to the Lluclla fault zone in the Sihuas valley. Exposure of the fault zone is poorer in the Molles valley, but the range front geometry suggests a steep (≥70°) SSW dip. Footwall igneous rocks include relatively coherent structural blocks separated by discrete cataclastic shear zones; typically, these zones strike N40–50°W and dip very steeply southwestward. As was the case in the Sihuas valley, hanging wall strata here are less penetratively deformed. However, they are deformed into macroscopic

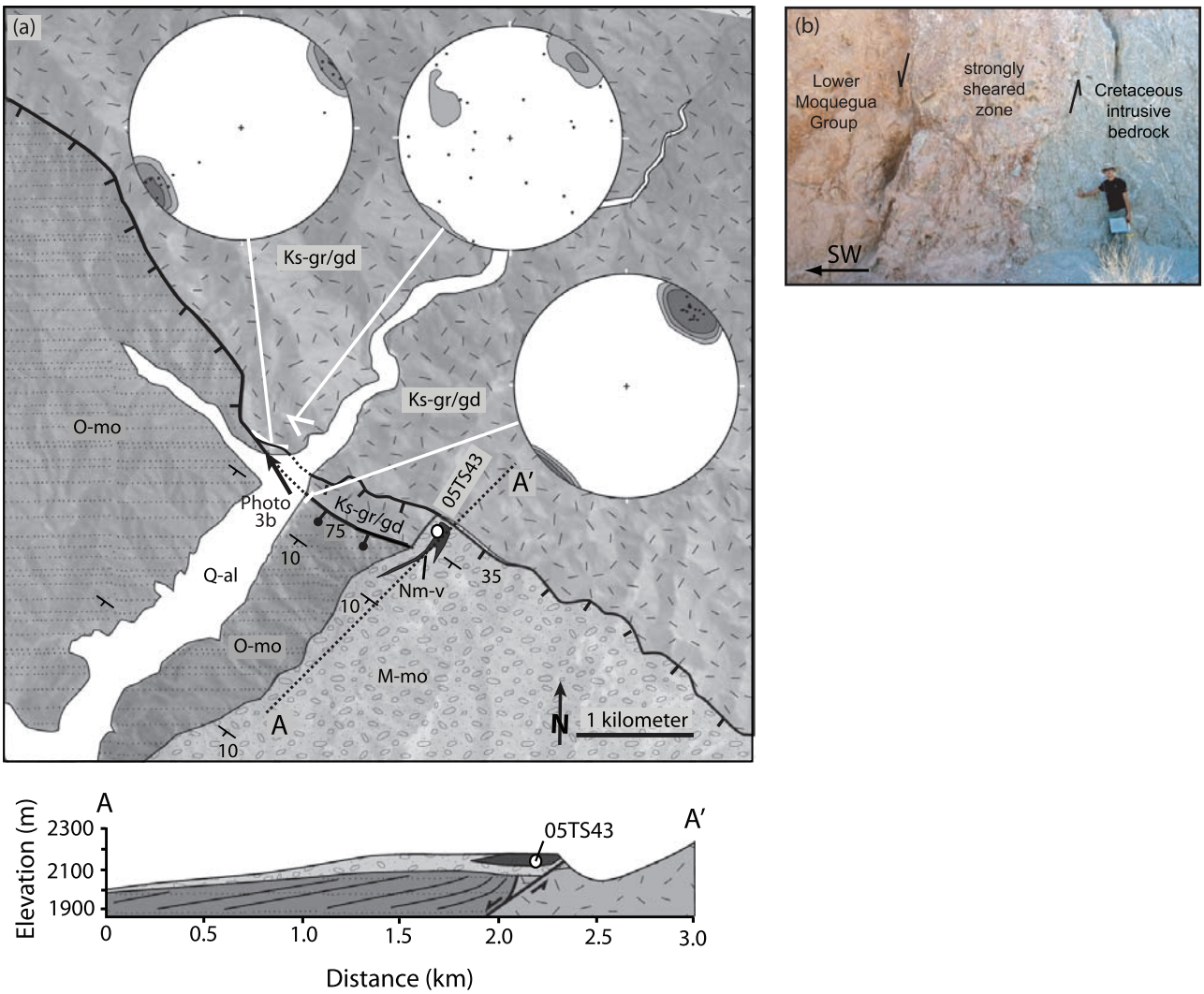

Figure 3. (a) Geological map of Sihuas valley near range front. Relief is from 15-m resolution band 3N from ASTER imagery. Stereonet plots show contour lines of poles to shear planes (and poles), and white bars indicate region from which shear planes were measured. White dot shows location for sample 05TS43 (16.12 ± 0.04 Ma), an undeformed ignimbrite intercalated with upper Moquegua sediments that cross the main shear zone. (b) Field photo reveals a normal fault contact dipping steeply to the southwest between the Moquegua group and Cretaceous intrusive bedrock. Arrow indicating location of field photo in Figure 3a also shows the orientation at which the photo was taken. Symbols include Ks-gr/gd, Cretaceous granite/granodiorite; O-mo, Oligocene lower Moquegua; M-mo, Miocene upper Moquegua; Q-al, Quaternary alluvium.

drag folds (Figure 4b) consistent with SW side down (i.e., normal sense) displacement on the fault zone. Again, rocks in the hanging wall and footwall cannot be matched, such that the local escarpment relief of ~600 m (based on the DEM) provides a minimum estimate of normal throw.

[13] An undeformed, fine-grained basaltic andesite (sample 04CC12) dated at 214 ± 44 ka and correlated with a phase of Pleistocene volcanism described by *Thouret et al.* [2007] overlies the fault trace in the Molles valley, giving a lower-age boundary to range front fault activity. Another constraint comes from a 14.11 ± 0.05 Ma tuff layer (sample 04CC13) within the upper Moquegua group gravels two kilometers south of the fault zone; an 18° southerly tilt of this unit along with the underlying gravels demonstrates post 14 Ma deformation of the Moquegua group. Additional coarse gravels with a regional slope of 1.5–2° to the south (within the range of slopes expected for such a deposit) overlie the deformed ignimbrite above an angular unconformity (Figure 4c). This implies that tilting occurred before deposition of the post-Moquegua gravels. These gravels are undated locally, but surface remnants project into the regional bajada surface to the south (Figure 1) that appears to be correlative with the Upper Miocene to Pliocene gravels of the Vitor valley (4.95 Ma, sample 07TS16

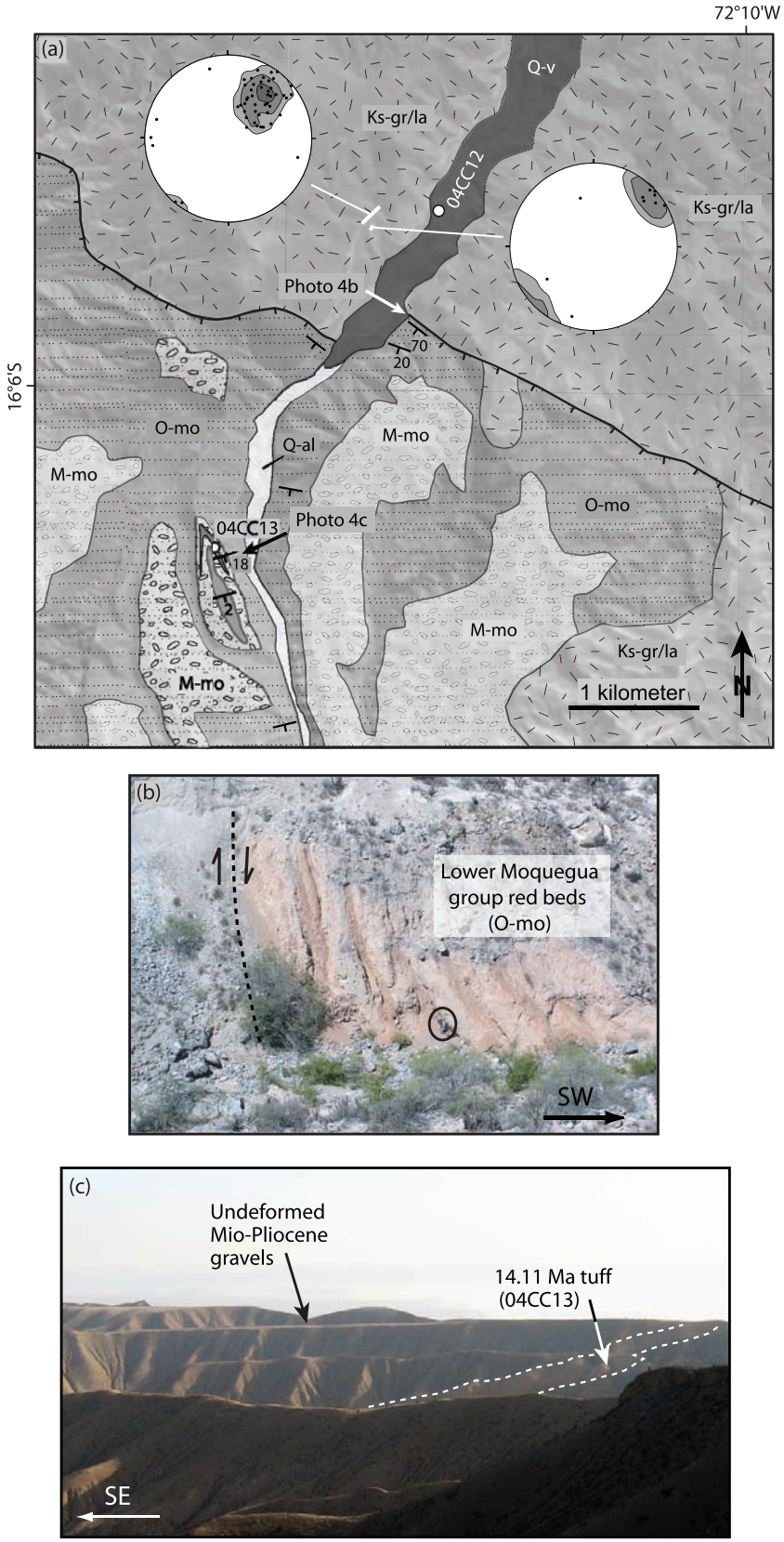
72°10'W
(a)
Q-v
Ks-gr/la
04CC12
Ks-gr/la
Photo 4b
70
20
16°6'S
O-mo
M-mo
Q-al
M-mo
O-mo
04CC13
Photo 4c
18
2
M-mo
M-mo
Ks-gr/la
1 kilometer
N
(b)
Lower Moquegua
group red beds
(O-mo)
SW
(c)
Undeformed
Mio-Pliocene
gravels
14.11 Ma tuff
(04CC13)
SE

Figure 4

(Figure 1 and Tables 2 and 3)) and the Sihuas valley (6.70, 6.79, and 6.96 Ma, sample 07TS15 (Figure 1 and Table 4)). This tentative correlation suggests that significant range front deformation occurred between 14.11 and ~7 Ma, with possible prior deformation as well. Modern canyons in the piedmont region were incised since ~7 Ma, perhaps in response to regional block uplift (phase 3 deformation).

3.3. Majes Valley

[14] The Colca-Majes River forms a 2-km-wide alluviated valley where it cuts through the WAE near the town of Aplao (Figure 5a). Topography is dramatic here, exposing a 600–800 m high morphological scarp that comprises much of the lower half of the WAE (Figure 5b). The interfluves west of the valley show a sequence of Moquegua sediments capped by the 16.1–13.2 Ma ignimbrites, forming the ramp morphology easily visible in satellite imagery. *Schildgen et al.* [2007] dated the most prominent capping ignimbrite in this region at 14.29 ± 0.04 Ma, which matches an age reported by *Thouret et al.* [2007] on the surface of this ignimbrite sheet farther to the northwest.

[15] Existing *INGEMMET* [2001] maps and our observations reveal that the piedmont region in this valley contains structures related to an early phase of contractile deformation. Several high-angle reverse faults south of the WAE cut both Mesozoic sedimentary bedrock and lower Moquegua red beds that were deposited before ~30 Ma (Sempere et al., presented paper, 2004). Near the town of Aplao, a reverse fault dipping approximately 70° NE places Jurassic bedrock over lower Moquegua red beds, but deformation decreases up section, with upper Moquegua group strata deformed into a monocline and erosionally stripped (Figure 5c). Two additional high-angle reverse faults 26 km south of the range front (16.202°S, 72.465°W) affect only lower Moquegua group sediments. An additional reverse fault 45 km south of the range front (16.359°S, 72.494°W) displays similar relationships, but deformation of upper Moquegua strata appears to be on the order of several hundred meters. An ash intercalated in the deformed Moquegua gravels is dated at 16.25 ± 0.10 Ma [*Thouret et al.*, 2007] and 16.26 ± 0.08 Ma (sample 07TS13). Given their steep dips, total shortening on these early contractile structures is likely to have been limited. We estimate reverse sense throw of the reverse faults to be on the order of 100–200 m.

[16] Much of the later deformation recorded in the region is extensional. Several high-angle normal faults deform upper Moquegua group and older units in this area. The most dramatic of these is the normal fault that marks the east-west striking range front (Figure 5b). Exposures of the fault itself are limited, but the 65° dip of the range front escarpment provides an approximate estimate for the fault dip. The total movement on this fault is difficult to assess, but is likely to be at least as great as the scarp height: 600–800 m. Although much of the faulted contact between intrusive bedrock to the north and Moquegua group sediments to the south is buried in landslide debris, limited exposures of upper Moquegua gravels close to the contact show beds dipping up to 30°S, indicating normal sense slip. Shear fabrics are cataclastic, and show no mylonites or evidence of plastic deformation, indicating shallow, low-temperature deformational conditions.

[17] A second, NW striking normal fault was mapped south of the range front. This steeply SW dipping structure cuts lower Moquegua group sediments and shows drag folds in sediments on the SW side of the fault suggesting normal sense displacement. Here the total throw on the fault cannot be determined precisely but may be as much as a few hundred meters. The fault continues southeastward, eventually residing entirely within the Moquegua stratigraphy. In this direction along strike, offsets diminish progressively and the fault eventually dies out into a SSW facing monocline that deforms upper Moquegua sediments. The NW end of the fault is buried beneath Quaternary valley fill sediments, so its relationship with the range-bounding fault is unclear. If the two merge, its offset may contribute to differential uplift of the Western Cordillera and central Andean Plateau relative to the piedmont. Alternatively, it may be related to a similarly oriented fault that follows the axis of the Chuquibamba valley, a large, landslide-filled tributary valley that extends NW of the WAE.

[18] A third extensional structure shown in the Majes map has a very different orientation. Striking NE and dipping steeply NW, this structure marks the southeastern flank of a small graben developed between it and the WAE scarp. Close to the Majes valley, the NE striking fault places upper Moquegua gravels dipping ~30°N, over pre–30 Ma lower Moquegua red beds dipping ~10° northward. Total throw in this area is no more than several hundred meters on the basis of stratigraphic relations. Farther southwest, this fault also dies out into a monocline facing northwestward that deforms the 16.1–13.2 Ma ignimbrite caprock in this region.

[19] Minimal activity on the range front fault in the western part of this area occurred after 14.29 Ma, as an overlapping ignimbrite sheet of that age shows only minor warping into a monocline. Farther to the east, deformation timing cannot be well constrained, as datable units have been

Figure 4. (a) Geological map of range front at Molles valley. Stereonets show poles and contours of poles of shear fractures north of the contact between intrusive bedrock and Moquegua group sediments. Locations of samples 04CC12 and 04CC13 are shown. Dark gray unit above sample 04CC13 represents angular unconformity between the tilted ash bed and undeformed Mio-Pliocene gravels (correlated with bajada surface and ashes 07TS15 (4.95 Ma) and 07TS16 (6.8–7 Ma)). (b) Red beds of lower Moquegua group warped upward near the fault zone. People are shown for scale (circled). (c) Undeformed gravels above tuff from which sample 04CC13 (14.11 Ma) was collected. Arrows indicating locations of field photos also show the orientation at which the photos were taken. Symbols in Figure 4a include Ks-gr/la, Cretaceous granite and latite; O-mo, lower Moquegua red beds; M-mo, upper Moquegua sands; Q-al, Quaternary alluvium.

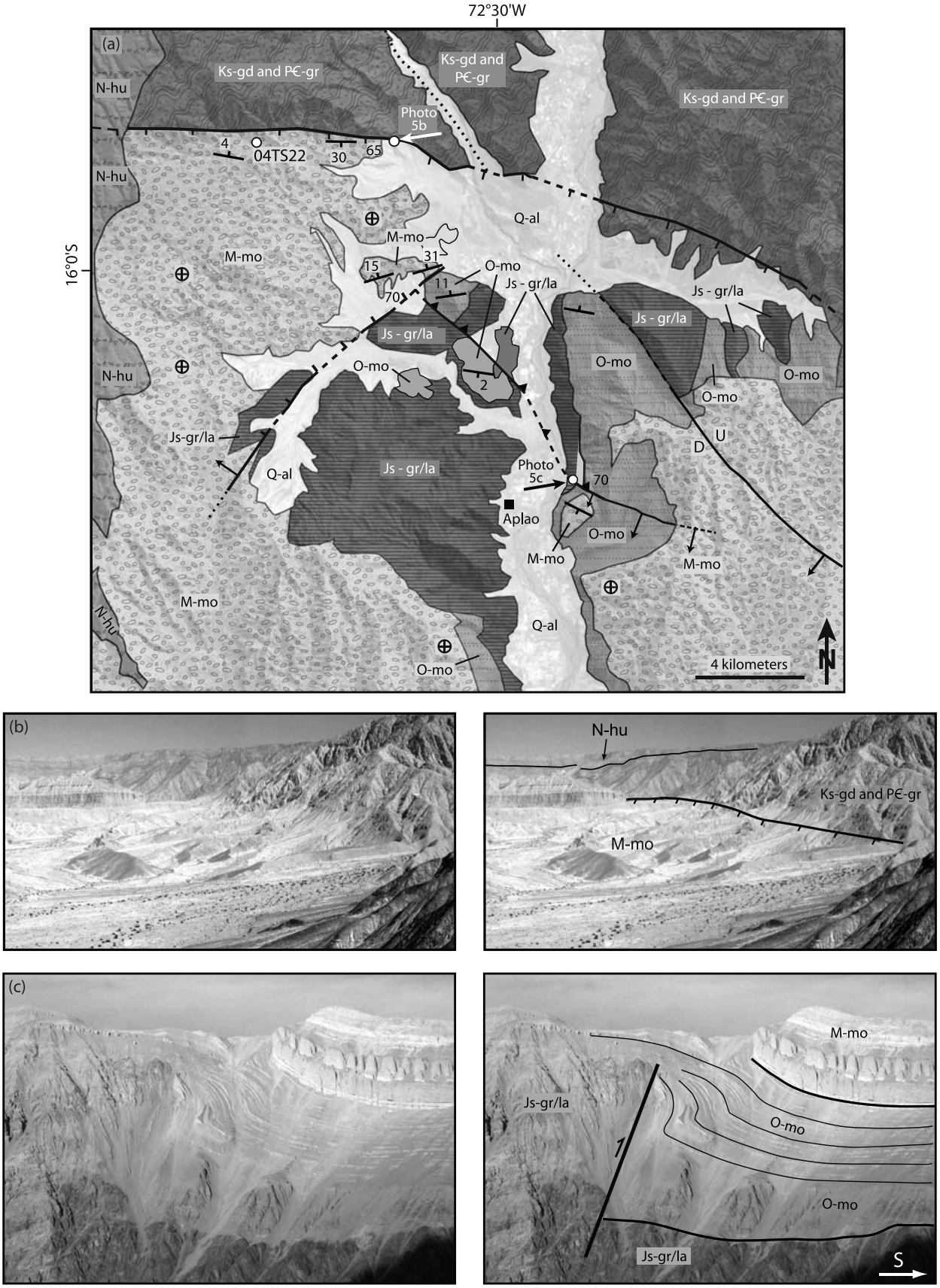
72°30'W
16°0'S
(a)
Ks-gd and P€-gr
N-hu
Photo 5b
4
04TS22
30
65
Q-al
M-mo
31
15
11
70
O-mo
Js - gr/la
2
U
D
Photo 5c
Aplao
4 kilometers
N
(b)
(c)
S

Figure 5

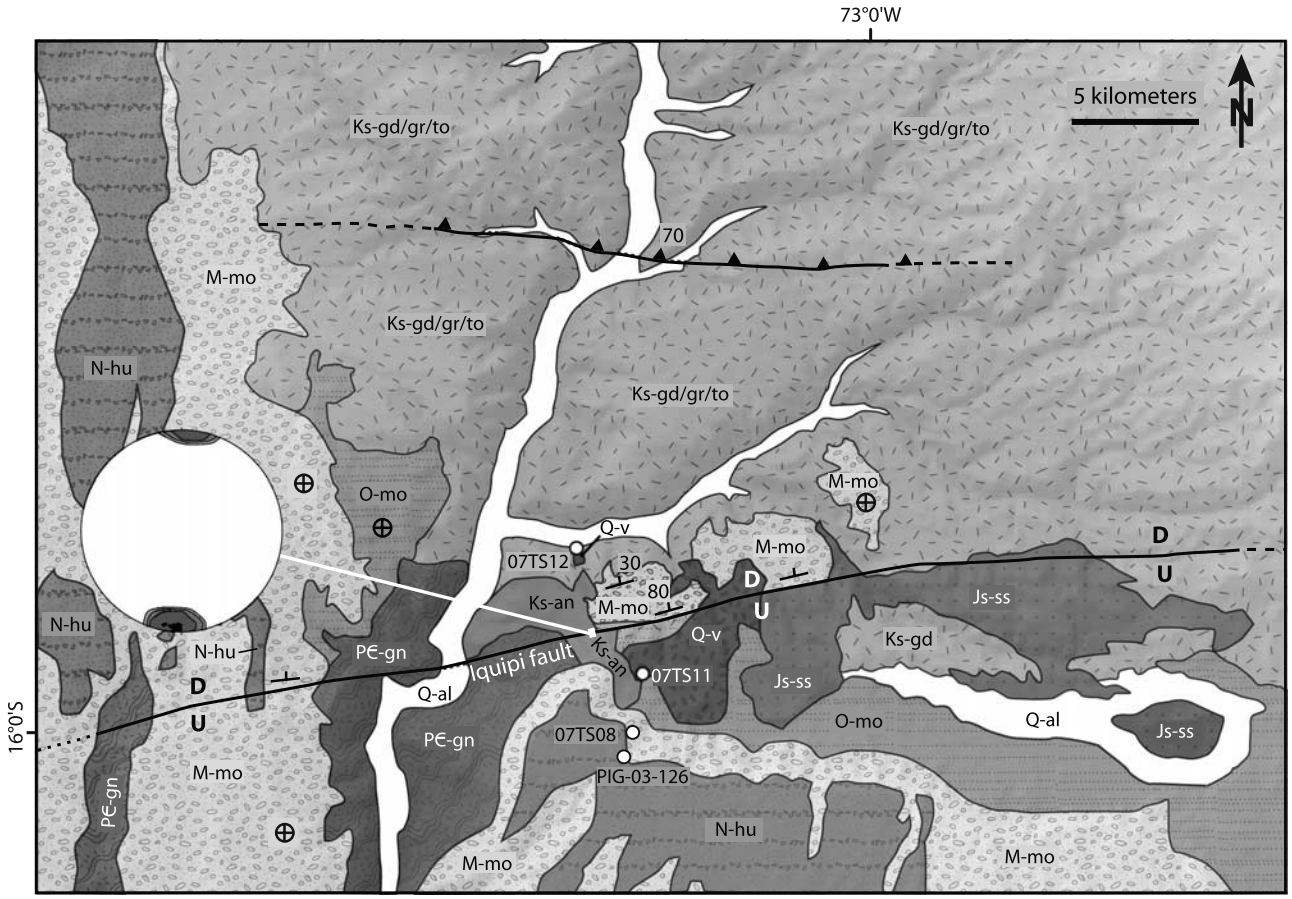

Figure 6. Ocoña valley geology map. Stereonet plots show contour lines of poles to shear planes (and poles), and white bars indicate region from which shear planes were measured. Sample PIG-03-126 was from a rhyolite capping the upper Moquegua sediments dated at 13.20 Ma [*Thouret et al.*, 2007]. Sample 07TS08 is an ash layer intercalated within upper Moquegua sediments (predominantly marine in this section) dated at 23.80 ± 0.16 Ma (Tables 2 and 3). Ignimbrite samples 07TS11 and 07TS12 were dated at 2.06 ± 0.05 Ma and 2.01 ± 0.03 Ma, respectively (Tables 2 and 3). Unit symbols include Q-v, Quaternary volcanic ash; Q-al, Quaternary alluvium; M-mo, Miocene upper Moquegua group conglomerates and marine sediments; O-mo, Oligocene lower Moquegua group red beds; Ks-gd, Cretaceous granodiorite; PC-gn, Precambrian gneiss.

eroded off the range front. The age of the youngest slip on other NW and NE striking normal faults are constrained only to be younger than the upper Moquegua units that they cut/deform.

3.4. Ocoña Valley

[20] The Cotahuasi-Ocoña River is the second major river in the region, draining through the 1-km wide Ocoña valley as it approaches the coast. Although there is no sharp range front in this region, several faults cut through the valley at a roughly equivalent position to that described in section 3.3 for the Majes valley (Figure 6).

[21] Similar to the previous three regions described, the Ocoña valley transect shows some evidence of early contractile deformation. A 70°N dipping, west striking shear zone was mapped in Cretaceous granitic rocks in the northern part of this area. Its dip direction and its burial beneath

Figure 5. (a) Geologic map of range front in Majes valley and field photos. Shown are locations of (b) field photo of range front escarpment, (c) field photo of the high-angle reverse fault near Aplao that cuts lower Moquegua group red beds and warps upper Moquegua group conglomerates, and sample 04TS22, an ignimbrite boulder derived from the Huaylillas ignimbrite. Arrows indicating locations of field photos also show the orientation at which photos were taken. Map symbols represent the following units: PC-gr, Precambrian granite; Js-gr/la, Jurassic granites and latites; Ks-gd, Cretaceous granodiorite; O-mo, Oligocene lower Moquegua group red beds; M-mo: Miocene upper Moquegua group conglomerates and gravels; Q-al, Quaternary alluvium. Faults are dotted where buried and are dashed where inferred.

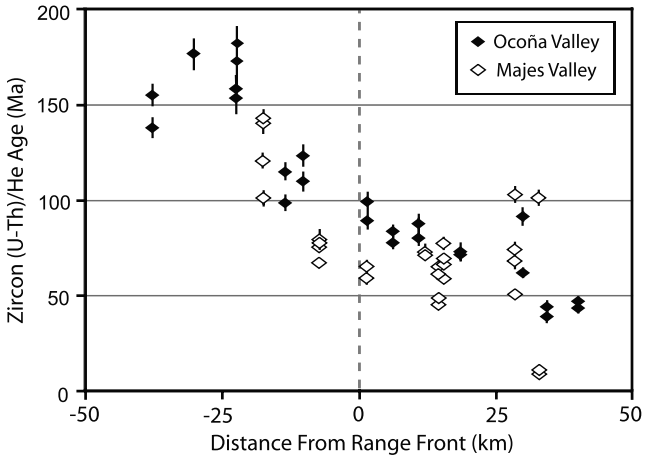

Figure 7. Zircon (U-Th)/He data from transects collected along the bottoms of Ocoña and Majes valleys. Data from Ocoña valley [*Schildgen et al.*, 2007] show increasingly young ages farther inland, with no clear discontinuities in age that would be indicative of significant movement on surface-breaking faults. Data from Majes valley are sparser and show poorer reproducibility but suggest a similar inland-younging trend, possibly including significant (~500-m) offset on the range front fault.

undeformed Moquegua units to the west (Figure 6) lead us to interpret it as a reverse fault with unknown throw.

[22] Later activity included slip on the Iquipi fault, an east-west striking high-angle structure that *Roperch et al.* [2006] described as accommodating left lateral motion prior to 15 Ma and probably before 25 Ma. Later movement on this fault also included a north side down component, as upper Moquegua group sediments step down ~100 m on the north side of the fault on the western rim of the valley. Total vertical slip on the fault is probably greater, however, as earlier movement likely contributed to the present-day 200 m escarpment in basement rocks (north side down) that can be traced along strike on satellite imagery for at least 35 km to the east of the valley and 15 km to the west of the valley (Figure 6).

[23] The Iquipi fault is characterized by a cataclastic shear zone at least several tens of meters thick. Shear orientations strike relatively uniformly subparallel to the Iquipi fault escarpment, with the differences in orientation possibly related to a rotational component of movement within the shear zone. Slickenlines are relatively rare on fault surfaces, however, this may be related to hydrothermal alteration. Bedrock is hydrothermally altered extending several hundred meters north of the shear zone (and in places has been extensively mined), but any deformation in this region is difficult to discern.

[24] Farther to the east, the fault escarpment is overlapped by the 14.29 Ma ignimbrite caprock dated by *Thouret et al.* [2007]. Although the fault trace is obscured, it projects into the steep range front in the Majes valley (see Figure 1, dashed ends of fault between the dotted rectangles representing Figures 6 and 5). If the fault traces do connect, the opposite senses of slip in the two regions suggest that a once throughgoing feature has subsequently been reactivated in distinct and potentially unrelated domains. The fault projects toward the west on satellite imagery, but is not clear west of the Caravelli valley. North of the Iquipi fault, a series of low-relief bedrock benches dominate the interfluve morphology. Elevations range from 1000 to 1800 m, or 500 to 1200 m above river level, and some benches have a thin veneer of sediment that has been mapped as Moquegua group by others [e.g., *Pecho*, 1983]. The Iquipi fault may represent the southern boundary of a half graben in the Ocoña valley. The flat bedrock benches perched at different levels north of the fault may represent smaller blocks that have experienced some movement, but there is no clear northern boundary to the extended region. Hence the deformation may be similar to what is exposed in the Majes valley, only without a sharp range front escarpment. Nonetheless, the swath profiles for this region ("ramp" in Figure 2) suggest north side up movement of ≥2 km relative to coastal regions on a monoclinal warp.

4. Thermochronologic Constraints on WAE Evolution

[25] Thermochronologic samples collected along the length of the Ocoña and Colca-Majes valleys (Figure 1) also provide insight into the style, magnitude, and timing of recent deformation. *Schildgen et al.* [2007] presented a valley bottom transect of (U-Th)/He zircon dates from the Ocoña valley, which showed no major discontinuities in the inland-younging trend of ages (Figure 7 and Table 4). Large discontinuities would be expected if significant offset were accommodated in a focused region. Small offsets can, however, be hidden within the data given analytical uncertainties and the spacing of sample locations. On the basis of an estimated background exhumation rate of 0.02 mm/a [*Schildgen et al.*, 2007], we can place upper bounds on the amount of fault displacement that could have occurred without perceptible disruption of the observed smooth age trend. A 100-m vertical displacement along a single fault would produce a 5 Ma discontinuity in the pattern of valley bottom transect data. Such a small change cannot be discerned given the uncertainty of the data and the spacing of samples. A 500-m vertical offset, however, would produce a 25 million year step, which, if present, would likely stand out on the trend.

[26] This analysis suggests that the total amount of movement across the range front in the Ocoña valley is likely to be less than 500 m subsequent to the helium closure ages of the youngest zircons defining this trend (~45 Ma). In the Majes valley, offset on the order of 500 m is feasible across the range front in this region postzircon closure (~60 Ma), but is unlikely to approach 1 km. Weighted mean apatite (U-Th)/He ages across the range front in the Majes valley are virtually indistinguishable (9.8 ± 0.3 Ma for sample 05TS15, 9 km south of the range front, and 10.2 ± 0.2 Ma for sample 05TS14, 11.5 km north of the range front

(Table 4)), suggesting that up to ~500 m movement across the range front occurred between ~45 and 10 Ma.

5. Distribution of Uplift

5.1. Deformation Across the WAE

[27] The importance of differential uplift across the WAE can only be assessed by evaluating the spatial distribution of total late Cenozoic surface uplift. Geological cross sections drawn from the range front to the coast (Figure 8) were made on the basis of mapped surface geology with locations shown in Figure 1. These highlight the transition from a gentle, ~70-km wide WAE with only minor fault disruption in the Cotahuasi-Ocoña region (Figure 8a), to a much more focused ~20-km wide WAE dominated by major faults in the Colca-Majes region (Figure 8b). Farther to the east, the WAE morphology appears to be intermediate between these two extremes (Figure 8c). These cross sections, as well as the zircon (U-Th)/He data (Figure 7), suggest that although focused deformation was probably greater in the Colca-Majes region (~1 km or less) compared to the Cotahuasi-Ocoña region (~500 m or less), the entire area is likely to have experienced significant differential uplift over a long-wavelength monocline.

[28] Constraints on the magnitude of this long-wavelength deformation are most easily derived from the Cotahuasi-Ocoña region. Apatite (U-Th)/He thermochronology data presented by *Schildgen et al.* [2007, 2008] imply at least 2.4–3 km of river incision in the deepest reaches of Cotahuasi-Ocoña canyon after ~9 Ma, providing a minimum estimate for the timing and magnitude of surface uplift that preceded incision in that region. The deepest reaches occur near the inland limit of the WAE, at ~100 km inland from the coast, or ~50 km north of Iquipi. Near Iquipi, Ocoña Canyon cuts to depths of 1.8 km through a 600-m thick pile of Moquegua group sediments and underlying bedrock (Figure 8a). The sediments include a marine layer with fossils including gastropods, pelecypods, and sea urchin remnants ~100m below the top of the section [*Huamán*, 1985; *Cruzado and Rojas*, 2007], implying ~1.7 km of piedmont uplift in that region since deposition of those sediments. An $^{40}Ar/^{39}Ar$ age of 23.80 ± 0.16 Ma on an ash above the marine layer (sample 07TS08 (Tables 2 and 3)) provides a limiting age. Moquegua group and younger gravels cap the section and form the top of a regional piedmont bajada surface that extends southward toward the coast. Within 16 km of the coast, these gravels onlap basement rocks of the beveled Coastal Cordillera at elevations of ~1000 m (Figure 8a), suggesting sea level was not far below at the time of deposition. Evidence of the former base level can be seen in swath profiles throughout southwestern Peru, where a dramatic rise in elevations to near 1000 m occurs within a few kilometers of the coastline (Figures 2 and 9). This in total implies that latest uplift of the Western Cordillera to current elevations involved both (1) at least 1.4–2 km of differential uplift of the cordillera relative to the piedmont across the WAE that was accommodated by both monoclinal folding and normal faulting and (2) ~1 km of coupled block uplift of the piedmont and the central Andean Plateau. Both phases of uplift dwarf the base level fall related to sea level change, the long-term amplitude of which is estimated to have dropped by ~40 m since the early Oligocene, with shorter-term variations on the order of 20–80 m [*Miller et al.*, 2005].

5.2. Block Uplift

[29] A better understanding of the block uplift component is best approached at the coast, to minimize effects of tectonics related to the WAE. At the outlet of the Colca-Majes River, near the town of Camaná, a road cut through fan delta sediments exposes beds dipping ~6° south, and an angular unconformity at 370 m elevation with flat-lying sediments above. We interpret these two units to be the foreset and topset beds of a single fan delta complex. Given that the contact between the beds was near sea level at the time of deposition and is likely to have experienced post-depositional subsidence and compaction, the coastal region has been uplifted at least 370 m since deposition. Sempere et al. (presented paper, 2004) described what we believe to be the same exposure as two units they named "Camana A" and "Camana B," and dated a tuff above the contact at 20.83 ± 0.06 Ma ($^{40}Ar/^{39}Ar$ on 3 biotite crystals). This correlates with zircon (U-Th)/He ages from a thin (~2–8 cm thick) reworked ash layer within the topset beds that yielded several Mesozoic to Paleozoic ages, but also two ages of 19.56 ± 0.46 Ma and 21.49 ± 0.52 Ma (sample 07TS01 (Table 4)). Because we interpret the dated material as reworked, the youngest dates should give maximum estimates for the age of the sediment, and may far exceed its age if the reworked ash was derived from a position relatively low in the Upper Moquegua stratigraphy. For this reason, we interpret the ~21 Ma ages from our work and Sempere et al. (presented paper, 2004) to be a maximum estimate for the timing of coastal uplift.

[30] The age of coarse gravels deposited at piedmont elevations in the Vitor and Sihuas valleys provide a much tighter constraint on the onset of coastal/piedmont uplift. The 4.95 Ma coarse gravels (dated by the intercalated tuff, sample 07TS16 (Tables 2 and 3)) perched high above the Vitor valley were likely deposited before significant incision of the Vitor River in the piedmont region. Slightly older ages were derived from lower in the gravel unit in the Sihuas valley, with youngest zircons from an intercalated ash yielding (U-Th)/He ages of ~6.7–7 Ma (Table 4). Similar limits for the onset of coastal/piedmont uplift are reported from small drainages in coastal northern Chile that cut through the piedmont surface. There, ashes intercalated in sediments overlying straths were dated at 6–6.4 Ma [*Sáez et al.*, 1999; *Hoke et al.*, 2007]. The preservation of knickpoints related to this coastal uplift in small drainages of northern Chile and southern Peru (Sihuas and Vitor valleys), but none in the largest valleys (Figure 9 and *Hoke et al.* [2007]) suggest a much slower response time to surface uplift in the smaller drainages. This may imply that the ~6–7 Ma limit derived from abandoned surfaces in small drainages may underestimate the age of coastal uplift. However, if, as

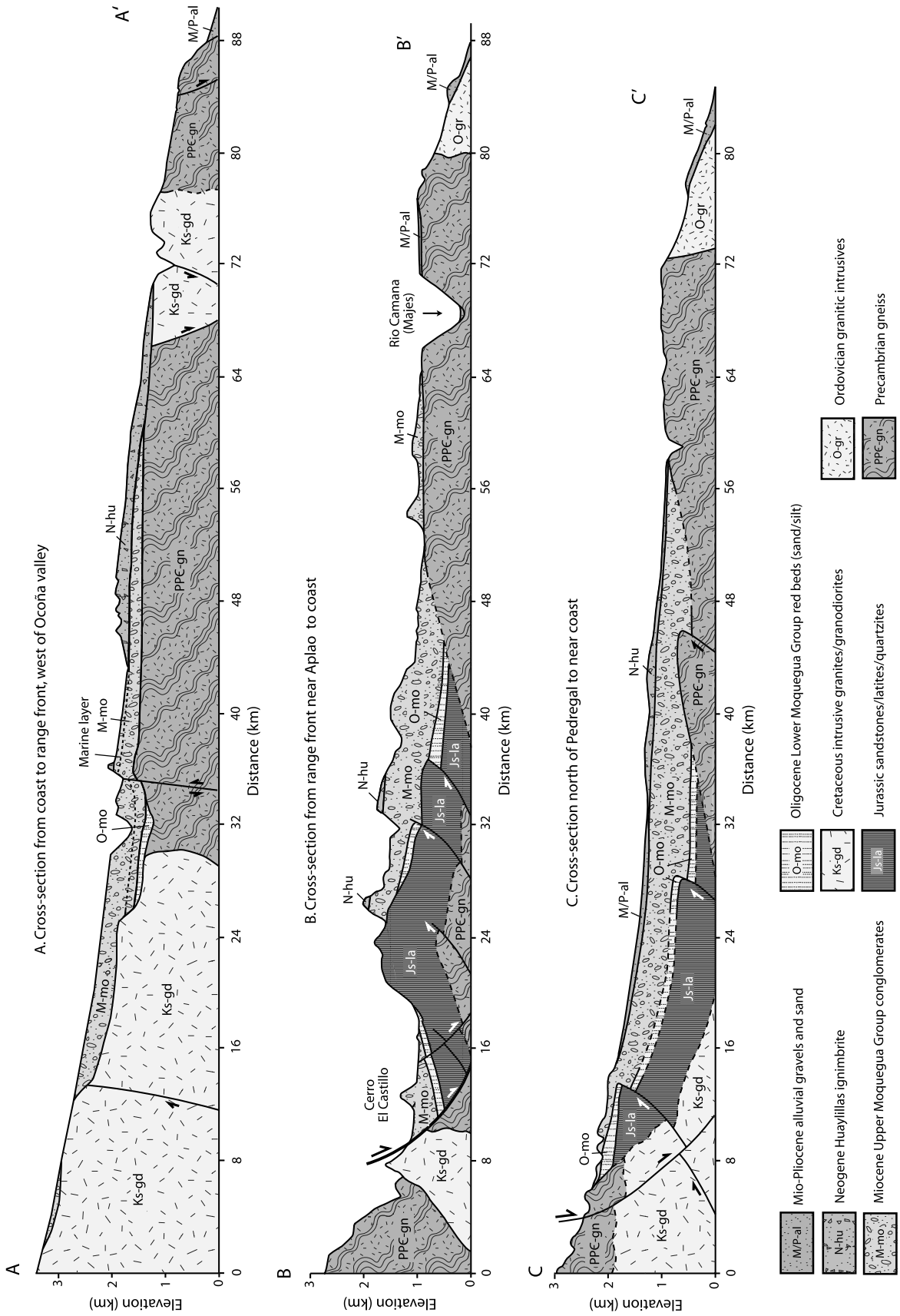

Figure 8. Geological cross sections based on mapped surface geology with locations shown in Figure 1. (a) Cross section A to A′ is west of the Cotahuasi-Ocoña valley, (b) cross section B to B′ is west of the Colca-Majes valley, and (c) cross section C to C′ is parallel to the Molles valley. Colors, symbols, and geological units used are identical to those shown in Figures 4–7. Vertical exaggeration in all cross sections is 3:1.

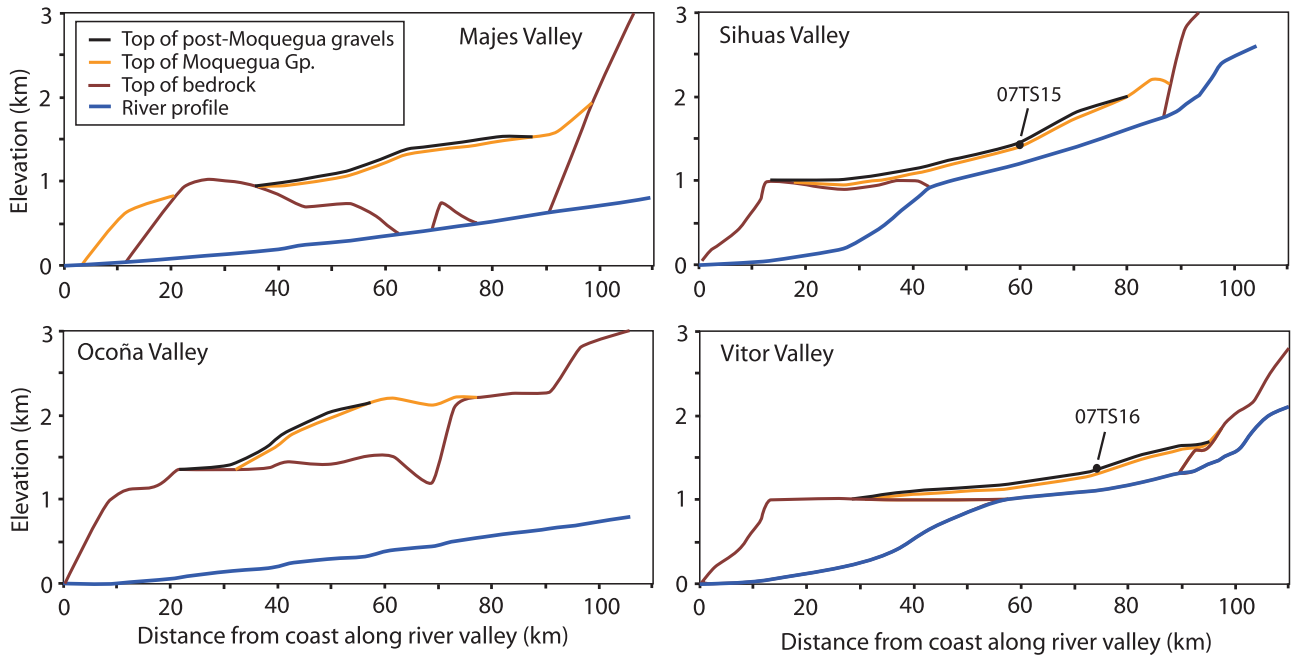

Figure 9. Profiles of river valleys (blue lines) and the exposed tops of bedrock (brown lines), Moquegua group sediments (orange lines), and post-Moquegua gravels (black lines), extracted from 1:100,000-scale topographic and geologic maps. Profiles were collected along the trace of the river valleys. Locations of samples 07TS15 (Table 4) and 07TS16 (Table 2), which are ashes intercalated within the post-Moquegua gravels, are shown.

we believe, abandonment of the high depositional surface requires only a small fraction of the total incision near the coast, even small drainages may provide reasonable age estimates. Incision into the surrounding surface has occurred upstream of the broad knick zone in both the Sihuas and Vitor valleys (Figure 9), implying that initial surface abandonment can be much faster than full propagation of a knickpoint through the drainage system.

6. Implications of Late Cenozoic Deformation and Uplift

[31] Deformation between the Western Cordillera and the southwest Peruvian coast reflects growth of the western margin of the central Andean Plateau. Our mapping demonstrates a long history of changing styles of structural accommodation. Early contractile deformation on high-angle reverse faults, similar in style and timing to that observed in northern and central Chile [e.g., *Muñoz and Charrier*, 1996; *García*, 2002; *Pinto et al.*, 2004; *Victor et al.*, 2004; *Farías et al.*, 2005] likely produced the high topography from which many of the major sedimentary units deposited in the piedmont region were derived. The later shift to a dominance of normal and monoclinal structures in southwest Peru by Middle Miocene time suggests a fundamental change in the stress regime that accompanied the latest two phases (phases 2 and 3) of surface uplift. Long-wavelength warping (~70-km wide between the coast and the high plateau) dominated in the Cotahuasi-Ocoña region, where prior periods of deformation appear to have had limited effects on the Precambrian basement and Cretaceous intrusive rocks that characterize the region (Figure 8a). Differential uplift transitioned 70 km to the southeast in the Colca-Majes region to being accommodated on steep faults and monoclines in a concentrated band ~20 km wide.

[32] The observation that late Neogene evolution of the WAE in southwest Peru was dominated by steep normal faulting and monoclinal warping has important implications for the growth kinematics of the western flank of the central Andean Plateau. Stress fields associated with such deformation are consistent with uplift driven by lower crustal flow in response to Brazilian Shield underthrusting beneath the eastern margin [e.g., *Isacks*, 1988; *Allmendinger et al.*, 1997; *Lamb et al.*, 1997; *Husson and Sempere*, 2003; *Gerbault et al.*, 2005; *Hindle et al.*, 2005] or by delamination of a thickened lower lithosphere as has been envisioned for the central Andean Plateau proper [e.g., *Kay and Kay*, 1993; *Garzione et al.*, 2006]. However, we have found no evidence of significant lateral growth of the plateau toward the Peru-Chile trench during plateau uplift. Moreover, we note that up to 1 km of the total plateau elevation in southwestern Peru must be attributed to wholesale uplift of the piedmont region along with the plateau. Thus, a significant component of uplift of the central Andean Plateau relative to sea level was not accommodated by surface deformation at the plateau margin, but instead may have been controlled by subduction zone processes.

[33] A number of subduction zone processes have been proposed to explain surface uplift along the western margin of the Andes. *Sébrier and Soler* [1991] argued that a cessation of slab retreat despite continued absolute westward movement of South America lead to short-lived late Tertiary compressional events. Although this may have been an important process for generating uplift in earlier stages of Andean development, the stress patterns accommodating uplift after ~14–16 Ma in southwest Peru are inconsistent with this process. Alternatively, progressive subduction erosion of lithosphere and associated thermal thinning can lead to isostatic uplift of the upper crust, as *Isacks* [1988] envisioned for the early middle Miocene phases of plateau uplift and as was described in greater detail by *Ranero and von Huene* [2000] and *von Huene and Ranero* [2003]. Such a process may be related to changes in the dip of the downgoing slab. In the Pampean flat slab region of the central Andes, from 27 to 33.5°S, the onset of basement block uplift shows remarkable correlation with the eastward migration of the volcanic arc associated with the shallowing slab dip [*Ramos et al.*, 2002]. In southwest Peru, the transition from a steeply (~30°) to shallowly (~15°) dipping slab occurs at 15.5°S [*Cahill and Isacks*, 1992; *Jordan et al.*, 1983], indicating that shallowing of the slab dip may have been an important factor in generating uplift.

[34] Subducted ocean floor features can similarly lead to uplift of the overriding plate, or even lead to changes in the slab dip. Several studies have noted the spatial correlation between the southern portion of the Peruvian flat slab region (extending from ~5 to 15.5°S) and the current ridge collision zone at 15°S [e.g., *Nur and Ben-Avraham*, 1981, 1983; *Pilger*, 1981; *McGeary et al.*, 1985]. *Gutscher et al.* [1999] attributed the flat slab region to the combined buoyancy of the subducted ridge (a feature almost 250 km wide and rising up to 1600 m above the surrounding seafloor) as well as that of a subducted "Lost Inca Plateau" beneath northern Peru. The oblique subduction angle of the Nazca plate beneath central Peru has lead to a c. 500 km southward migration of the collision zone between the Nazca Ridge and the coast since its initial collision near 11.2°S at c. Eleven Ma [*Hampel*, 2002; *Clift et al.*, 2003]. Although there is no clear evidence today that subducted oceanic features generated surface uplift in our field area in southwestern Peru (south of the current ridge collision zone), the regional patterns of deformation we have described are consistent with subduction processes having played a significant role in the evolution of the western margin of the Andean Plateau between the coast and the Western Cordillera.

7. Conclusions

[35] Structural mapping and thermochronological studies in southwest Peru provide important insights into the history of deformation and its relation to surface uplift between the coast and the western margin of the central Andean Plateau. Changing stress regimes in the developing plateau led to different generations of reverse faulting, normal faulting, long-wavelength monoclines, and regional block deformation that accommodated uplift of the plateau relative to the coast. Early contractile deformation was accommodated primarily on a series of west vergent reverse faults that affected Oligocene to Early Miocene sediments as well as older units. In the Ocoña valley, these structures are dispersed throughout the ~70-km wide fore-arc region and each accommodated uplift on the order of 100–300 m. Early movement of structures farther to the east is less well constrained, but is likely to have been more focused in a ~20-km wide zone along the sharp range front escarpment. By Middle Miocene time, deformation was dominated by normal faulting and broad monoclinal warping. Normal fault movement likely contributed to the sharp morphological expression of the range front seen today in the Majes valley and to the southeast. On the west side of the Majes valley and in the Ocoña valley, extension produced a series of grabens. Total post 16 Ma uplift of inland regions relative to coastal regions accommodated on discrete faults near the WAE is most likely on the order of several hundred meters, but cannot exceed 1 km. This implies that latest uplift of the Western Cordillera to current elevations involved both (1) at least 1.4–2 km of differential uplift of the cordillera relative to the piedmont across the WAE that was accommodated by both monoclinal folding and normal faulting starting no later than ~9 Ma and (2) ~1 km of coupled uplift of the piedmont and the central Andean Plateau that started after ~5 Ma. Because incision in the Ocoña valley ended at 2.2 Ma on the basis of the $^{40}Ar/^{39}Ar$ age of a lava flow on the present valley floor [*Schildgen et al.*, 2007], both phases of deformation must have been completed by that time.

[36] The changes in deformation patterns through time on the western margin of the central Andean Plateau likely reflect changing dynamics of the evolving plateau. Early contraction in the central Andes led to extensive upper crustal shortening and thickening. A major phase of uplift that started at ~9–10 Ma and ended by 2.3 Ma [*Schildgen et al.*, 2007, 2008; *Thouret et al.*, 2007] was accompanied by an apparent change in the style of structural accommodation along the western margin of the plateau in southwest Peru, with uplift of the plateau relative to the piedmont accommodated by structures that resulted in little, if any, propagation of the plateau toward the Peru-Chile trench. Processes that have been envisioned to explain this late Neogene uplift include lower crustal flow into the western part of the central Andean Plateau, various forms and geometries of lithospheric delamination, and a shallowing of subduction angle, and an increase in friction on the plate boundary [*Lamb and Davis*, 2003]. While our results alone do not definitively negate any of these hypotheses, the balance of data available at this time lead us to favor a combination of processes to explain the evolution of the western margin. Lower crustal flow and/or lithospheric delamination can be invoked to generate the ~1.4–2 km of differential uplift of the plateau relative to the piedmont, but these processes are unlikely to generate uplift of cold, thin, crust near the subduction zone. For this reason, we believe subduction zone processes such as subduction erosion, subduction of an oceanic feature, and/or

changes in the slab dip must also have played a significant role in generating uplift.

Appendix A

A1. The $^{40}Ar/^{39}Ar$ Geochronology Methods

[37] Fresh crystals of biotite and feldspar were hand-picked from the 500–1000 μm diameter fraction of crushed ash samples. Biotite crystals were ultrasonically cleaned in high-purity water and ethanol, ground in a mortar and pestle to remove altered grain edges, and ultrasonically cleaned a second time prior to packaging in Al foil packets. Feldspars were etched in HCl and HF prior to ultrasonic cleaning in high-purity water and ethanol, followed by packaging in Al foil packets. The groundmass sample was crushed to 250–500 μm diameter, etched with HCl, cleaned in high-purity water and ethanol, and packaged into Cu foil packets. All samples were encapsulated in quartz vials for irradiation. Samples were irradiated at the McMaster University reactor along with flux monitor TCR-2a sanidine (28.34 Ma [*Renne et al.*, 1998]) and synthetic salts to permit corrections for interfering nuclear reactions. Vertical monitoring of the neutron flux resulted in J values known to better than 0.2–0.3%.

[38] Gas was liberated from crystals after either (1) total fusion by laser heating of feldspar and biotite or (2) incremental heating of the groundmass packet. Total laser fusion of single feldspar or biotite grains was accomplished by loading crystals into copper pan wells with complete degassing via heating for 15 s with a Coherent Innova 210 Ar ion laser or a Coherent 20W Ar ion laser beam that encompassed the well diameter and converted the fragments to roughly spherical glass beads. The groundmass sample was incrementally heated in a vacuum furnace in 14 steps, 6 of which (incorporating 69% of the total released gas) were used in the age calculation.

[39] The evolved gas was purified with a series of metal alloy getters and analyzed on the Massachusetts Institute of Technology MAP 215–50 mass spectrometer with an electron multiplier. Total system blanks were measured at the beginning of each analytical session, between sets of five or ten total fusion hornblende analyses, and between sets of two to six laser spot or incremental heating analyses depending on blank reproducibility. Mass fractionation was monitored by routine analysis of laboratory air over the duration of the analytical campaign. Isotopic measurements were reduced using the ArArCALC routines of *Koppers* [2002] and corrected for system blanks, mass fractionation, and neutron-induced interferences. Apparent $^{40}Ar/^{39}Ar$ ages were calculated using decay constants recommended by *Steiger and Jäger* [1977] and assuming an initial $^{40}Ar/^{36}Ar$ ratio of 295.5. Age uncertainties throughout this paper include errors associated with blank and sample isotopic measurements, fractionation, interfering reactions, and J. Laser spot ablation results are cited as weighted mean dates with uncertainties reported at twice the weighted standard error of the mean. For samples with weighted mean dates characterized by a MSWD (mean square weighted deviate) >1, scatter is assumed to be greater than the contribution from analytical errors, and errors were multiplied by the square root of the MSWD [*York*, 1968]. Inverse isotope correlation diagrams were constructed using a *York* [1968] regression analysis to compute isochron dates and initial $^{40}Ar/^{36}Ar$ ratios. For the incremental heating experiments, plateau dates are calculated using three or more consecutive steps comprising at least 50% of the total $^{39}Ar_K$ released and are considered statistically significant if the MSWD of the mean lies within the 2 sigma uncertainty of the expected value of 1.0.

A2. (U-Th)/He Thermochronology Methods

[40] For apatite and zircon separation, samples were crushed using only a jaw crusher to maximize the yield of whole apatite grains, followed by standard Wilfley table, magnetic, and heavy liquid mineral separation techniques. Apatites were inspected for inclusions and photographed under 150x magnification using a Zeiss V.12 Discovery microscope. Crystal dimensions of euhedral, inclusion-free grains were measured prior to loading single grains into small 0.027″ OD × 0.04″ long Pt tubes for apatite, and Nb tubes for zircon. Tubes were loaded into a 25 spot sample holder of an ASI Alphachron U/Th-He dating system ("miniHe") with 2 blank tubes and 3 tubes loaded with an age standard. Single shards of Durango apatite were used as age standards for apatite samples and a combination of Durango apatite and Fish Canyon zircon were used for zircon samples. Helium was released from apatite by laser heating with a 980nm diode laser for 5 min at 9 Amps, and from zircon by laser heating for 10 min at 20 Amps. The gas was spiked with ^3He and exposed to a hot SAES NP-10 getter for 2 min, after which the gas was expanded into a Pfeiffer–Balzers Prisma Quadrupole with a range of 0–100 amu, Channeltron electron multiplier, and a faraday detector that also has a room temperature SAES NP-10 getter in the vacuum chamber. The ASI Alphachron does not have a He cryogenic refrigerator to concentrate the sample gas before inlet into the quadrupole mass spectrometer as the volume of the extraction line is so small that the gain in volume and gas let into the mass spectrometer chamber would be minimal.

[41] Helium blanks were determined by heating empty Pt and Nb tubes following apatite and zircon procedures. On average the blanks were between 0.045 ± 0.009 fmol for both the apatite and zircon procedures. For most apatite analyses, the sample to blank ratios were well in excess of 10, with most ≥100, while for zircon analyses the lowest sample to blank ratios were ~920, with the majority of the sample to blank ratios in the 10^3–10^4 range.

[42] To analyze the $^4He/^3He$ composition of the gas, four masses were monitored during analysis: Mass 1 as a proxy for HD contributions to the mass 3 peak, Mass 3 for ^3He, Mass 4 for ^4He and Mass 5 for the background. The HD contribution to the ^3He peak is on average 0.03%, but in some cases has been as high as 0.13%. ^4He concentrations were calculated by comparing the sample $^4He/^3He$ to a set of standard analyses run prior to and after the sample analysis. Short-term (5–10 standard analyses) reproducibility is on

the order of 0.03–0.05%, while the long-term (complete sample holder run) reproducibility is on the order of 0.05–0.08%. The composition of the ^{4}He standard gas tank is known to 1.2%, which represents the largest contribution to the error in this part of the analytical process.

[43] After initial He extraction, all samples where reextracted with the same analytical procedure. In all cases apatite grains reextracted perfectly to blank levels, while zircons were reextracted until helium yields were less than between 0.5 and 1% of the original extracted gas. On occasion this required multiple reextractions. The reasons for this phenomenon are poorly understood, but it does not negatively affect the final age calculated [e.g., *Reiners*, 2005].

[44] Following He measurement, the metal tubes containing the grains were unloaded and digested for U and Th analysis on an inductively coupled plasma–mass spectrometry (ICP-MS). Apatites were dissolved in concentrated HNO_3 following procedures outlined by *Evans et al.* [2005]. Pt packages containing the apatites were transferred to 1.5 ml polypropylene microvials to which a 25 μl microliter ^{235}U and ^{230}Th spike solution made up in 50% distilled ultra pure HNO_3 was added. The ^{235}U and ^{230}Th spike solution has a concentration of 15ng/ml and 5ng/ml, respectively. Samples were then sonicated for 15 min and rested for 4 h to allow for apatite dissolution. After this, samples were diluted with 325 μl of Milli-Q 18.2 MegaOhm polished water containing <0.2% Triton (an industrial solvent that aids to keep Th mobile in the ICP inlet system) to make up the final solution for analysis.

[45] Zircon dissolution requires the use of concentrated HF, HNO_3, and HCl combined with higher than ambient temperature and pressures [*Reiners et al.*, 2002; *Reiners*, 2005]. Because the zircon digestion procedure also dissolves Pt or Nb, we used Nb tubes for zircon to avoid severe PtAr interferences on the U mass spectrum in the ICP-MS. The high melting point of Nb precludes melting during laser heating, and it's low atomic mass means that NbAr complexes do not cause interferences on the U mass spectrum. The Nb tubes containing the extracted samples were transferred into Teflon microvials (0.35 ml) and 50 μl of the same spike used for the apatite analysis was added together with 300 μl of distilled ultra pure concentrated HF. The vials were then put into Teflon liners of 125 ml Parr digestion vessels, which each hold up to 10 vials. For pressure balance, 10 ml of trace metal grade concentrated HF and 0.45 ml trace metal grade concentrated HNO_3 were added to the liner. The digestion vessels were heated at 225°C for 72 h, after which the samples were heated to dryness at low (60–70°C) heat. Samples were then put back in the Parr digestion vessels with 300 μl of distilled ultra pure concentrated HCl added to each vial, 9 ml of trace metal grade concentrated HCl was added to the liner, and the vessel was heated at 200°C for 24 h. Following this, samples were again heated to dryness before adding 25 μl of distilled ultra pure concentrated HF and 200 μl of distilled ultra pure concentrated HNO_3. Sample vials were then closed and heated at 60–70°C for 30 min before the contents were transferred to larger 5 ml polypropylene vials holding 3 ml of Milli-Q 18.2 MegaOhm polished water to make up the final solution of 0.8% HF and 6% HNO_3 for analysis.

[46] The solutions were analyzed on a Thermo X series quadrupole ICP-MS in the Keck Lab at ASU, using a micronebulizer with an uptake rate of 100 μl/minute. The analytical procedure consisted of 7 and 10 cycles for apatite and zircon solutions, respectively, with each cycle entailing 150 sweeps of ^{230}Th, ^{232}Th, ^{235}U, ^{238}U and ^{234}U, which can be used as a proxy for detection of isobaric interferences on the U mass spectrum for platinum argides. Analyses were standardized by analyzing a spiked standard (SPST) solution, which is a mixture of the same spike solution used for the apatite and zircon solutions and a U and Th standard of known concentration. For SPST solutions run with the apatite samples, 25 μl of spike was added to 25μl of the standard solution, which had a concentration of 25ng/ml of U and Th in 4% HNO_3, which was then diluted with 300 μl Milli-Q 18.2 MegaOhm polished water also containing the Triton to make the final solution. For zircons, 50 μl of spike was mixed with 50 μl of the standard solution, 100 μl of distilled ultra pure concentrated HNO_3, and 25 μl of distilled ultra pure concentrated HF. The solution was then diluted with 3 ml of Milli-Q 18.2 MegaOhm polished water to make up the final solution of 0.8% HF and 4–6% HNO_3 for analysis. One SPST solution was also added to each Parr digestion vessel to monitor for any effects of contamination during the Parr digestion process. So far we have not encountered any major differences between the SPST solutions that have gone through the Parr digestion process and those that are prepared without going through that process. Reproducibility of the spiked standard analysis is on the order of 1.0% for U and 1.4% for Th.

[47] Total process blanks were determined by taking the empty Pt and Nb tubes used to determine the He blanks and process them with the samples through the preparation steps for U and Th analysis. Average Pt tube blanks for the apatite procedure are 0.65 ± 0.04 pg (1σ standard error) U and 0.41 ± 0.05 pg (1σ standard error) Th, while average Nb tube blanks are higher at 2.9 ± 0.4 pg (1σ standard error) U and 3.0 ± 0.9 pg Th (1σ standard error).

[48] Ages were calculated with an iterative process using blank corrected He, Th, and U values. Raw ages were corrected for alpha ejection effects following methods described by *Farley et al.* [1996] and *Farley* [2002] for apatite and by *Hourigan et al.* [2005] and *Reiners* [2005] for zircon. The average age determined for DURANGO apatite in the Noble Gas Geochemistry and Geochronology Laboratory at ASU is 31.89 ± 1.07 (1σ SD) Ma with a standard error of 0.09 Ma (n = 141), which is in good agreement with all shards included with the apatite and zircon samples of this study. A total of 9 Fish Canyon Tuff zircon grains were analyzed and gave an average age of 28.40 ± 1.84 (1σ SD) Ma with a standard error of 0.45 Ma (n = 17). Analytical errors propagated throughout the process amount to 1.5–2.5% (1σ). Errors associated with the alpha ejection correction were not directly determined, but following discussions by *Farley et al.* [1996], *Spotila*

et al. [1998], and *Hourigan et al.* [2005], they are estimated to push the total error for the method to 3–5% 1σ. Alpha ejection corrections were made assuming a homogeneous U and Th distribution, which, especially for zircon, may not be realistic and can lead to significant additional scatter in the age data [e.g., *Hourigan et al.*, 2005].

[49] **Acknowledgments.** We thank Tyson Smith and Julie Bradley for help with fieldwork; Greg Hoke, Gerhard Wörner, and Silvan Hoth for discussions; Mariela Perignon for help with sample preparation; Javier Bustamante, Marc Goddard, and Gian Marco Vellutino for help with field and sampling logistics; and Bill Olzscheski for help with $^{40}Ar/^{39}Ar$ analyses. Comments from two anonymous reviewers helped to improve the manuscript. This work was supported by the National Science Foundation Tectonics Division grant EAR-0409359.

References

Allmendinger, R. W., T. E. Jordan, S. M. Kay, and B. L. Isacks (1997), The evolution of the Altiplano-Puna plateau of the central Andes, *Annu. Rev. Earth Planet. Sci.*, *25*, 139–174.

Barke, R., and S. Lamb (2006), Late Cenozoic uplift of the eastern Cordillera, Bolivian Andes, *Earth Planet. Sci. Lett.*, *249*, 350–367, doi:10.1016/j.epsl.2006.07.012.

Berry, E. W. (1939), *The Fossil Flora of Potosi, Bolivia*, *John Hopkins Univ. Stud. Geol.*, *13*, 67 pp.

Cahill, T., and B. L. Isacks (1992), Seismicity and shape of the subducted Nazca plate, *J. Geophys. Res.*, *97*, 17,503–17,529, doi:10.1029/92JB00493.

Clift, P. D., I. Pecher, N. Kukowski, and A. Hampel (2003), Tectonic erosion of the Peruvian forearc, Lima Basin, by subduction and Nazca Ridge collision, *Tectonics*, *22*(3), 1023, doi:10.1029/2002TC001386.

Cruzado, G. H., and M. C. Rojas (2007), Estratigraphía de la Fm. Moquegua Superior en el area del cerro Cuno Cuno y Pampas del Gramadal, tesis de grado, 95 pp., Univ. Mayor de San Marcos, Lima.

Evans, N. J., J. P. Byrne, J. T. Keegan, and L. E. Dotter (2005), Determination of uranium and thorium in zircon, apatite, and fluorite: Application to laser (U-Th)/He thermochronology, *J. Anal. Chem.*, *60*(12), 1159–1165, doi:10.1007/s10809-005-0260-1.

Farías, M., R. Charrier, D. Comte, J. Martinod, and G. Hérail (2005), Late Cenozoic deformation and uplift of the western flank of the Altiplano: Evidence from the depositional, tectonic, and geomorphologic evolution and shallow seismic activity (northern Chile at 19°30′S), *Tectonics*, *24*, TC4001, doi:10.1029/2004TC001667.

Farley, K. A. (2002), (U-Th)/He dating: Techniques, calibrations, and applications, in *Noble Gases in Geochemistry and Cosmochemistry*, *Rev. Mineral. Geochem.*, vol. 47, edited by D. Porcelli, C. J. Ballentine, and R. Wieler, pp. 819–844, Mineral. Soc. of Am., Washington, D. C.

Farley, K. A., R. A. Wolf, and L. T. Silver (1996), The effects of long alpha-stopping distances on (U-Th)/He ages, *Geochim. Cosmochim. Acta*, *60*(21), 4223–4229, doi:10.1016/S0016-7037(96)00193-7.

García, M. (2002), Evolution Oligo-Miocene de L'altiplano Occidental (arc et avant-arc du nord Chile, Arica): Tectonique, volcanisme, sédementation, géomorphologie et bilan érosion-sédementation, Ph.D. thesis, 118 pp., Univ. Joseph Fourier, Grenoble, France.

Garzione, C. N., P. Molnar, J. C. Libarkin, and B. J. MacFadden (2006), Rapid late Miocene rise of the Bolivian Altiplano: Evidence for removal of mantle lithosphere, *Earth Planet. Sci. Lett.*, *241*, 543–556, doi:10.1016/j.epsl.2005.11.026.

Gerbault, M., J. Martinod, and G. Herail (2005), Possible orogeny-parallel lower crustal flow and thickening in the central Andes, *Tectonophysics*, *399*, 59–72, doi:10.1016/j.tecto.2004.12.015.

Ghosh, P., C. N. Garzione, and J. M. Eiler (2006), Rapid uplift of the Altiplano revealed through ^{13}C-^{18}O bonds in paleosol carbonates, *Science*, *311*(5760), 511–515, doi:10.1126/science.1119365.

Graham, A., K. M. Gregory-Wodzicki, and K. L. Wright (2001), Studies in neotropical paleobotany. XV. A Mio-Pliocene palynoflora from the eastern Cordillera, Bolivia: Implications for the uplift history of the central Andes, *Am. J. Bot.*, *88*(9), 1545–1557.

Gregory-Wodzicki, K. M. (2000), Uplift history of the central and northern Andes: A review, *Geol. Soc. Am. Bull.*, *112*(7), 1091–1105, doi:10.1130/0016-7606(2000)112<1091:UHOTCA>2.3.CO;2.

Gutscher, M. A., J. L. Olivet, D. Aslanian, J. P. Eissen, and R. Maury (1999), The "lost Inca Plateau": Cause of flat subduction beneath Peru?, *Earth Planet. Sci. Lett.*, *171*, 335–341, doi:10.1016/S0012-821X(99)00153-3.

Hampel, A. (2002), The migration history of the Nazca Ridge along the Peruvian active margin: A re-evaluation, *Earth Planet. Sci. Lett.*, *203*, 665–679, doi:10.1016/S0012-821X(02)00859-2.

Hindle, D., J. Kley, O. Oncken, and S. Sobolev (2005), Crustal balance and crustal flux from shortening estimates in the central Andes, *Earth Planet. Sci. Lett.*, *230*, 113–124, doi:10.1016/j.epsl.2004.11.004.

Hoke, G. D., and C. N. Garzione (2008), Paleosurfaces, paleoelevation, and the mechanisms for the latest Miocene topographic development of the Altiplano Plateau, *Earth Planet. Sci. Lett.*, *271*, 192–201.

Hoke, G. D., B. L. Isacks, T. E. Jordan, N. Blanco, A. J. Tomlinson, and J. Ramezani (2007), Geomorphic evidence for post-10 Ma uplift of the western flank of the central Andes 18°30′–22°S, *Tectonics*, *26*, TC5021, doi:10.1029/2006TC002082.

Hourigan, J. K., P. W. Reiners, and M. T. Brandon (2005), U-Th zonation-dependent alpha-ejection in (U-Th)/He chronometry, *Geochim. Cosmochim. Acta*, *69*(13), 3349–3365, doi:10.1016/j.gca.2005.01.024.

Huamán, D. (1985), Evolution tectonique Cénozoique et néotectonique du piémont pacifique dans la région d'Aréquipa (Andes du sud du Pérou), Ph.D. thesis, 220 pp., Univ. Paris XI, Orsay, France.

Husson, L., and T. Sempere (2003), Thickening the Altiplano crust by gravity-driven crustal channel flow, *Geophys. Res. Lett.*, *30*(5), 1243, doi:10.1029/2002GL016877.

Instituto Geológico Minero y Metalúrgico (INGEMMET) (2001), Mapa geologico del cuadrangulo de Caraveli, scale 1:100,000, Lima.

Isacks, B. L. (1988), Uplift of the central Andean Plateau and bending of the Bolivian orocline, *J. Geophys. Res.*, *93*, 3211–3231, doi:10.1029/JB093iB04p03211.

Jordan, T. E., B. L. Isacks, R. W. Allmendinger, J. A. Brewer, V. A. Ramos, and C. J. Ando (1983), Andean tectonics related to geometry of subducted Nazca Plate, *Geol. Soc. Am. Bull.*, *94*(3), 341–361, doi:10.1130/0016-7606(1983)94<341:ATRTGO>2.0.CO;2.

Jordan, T. E., C. Mpodozis, N. Blanco, G. D. Hoke, and P. L. Nester (2006), Surface uplift of the western slope of the Puna segment of the central Andean Plateau, *Geol. Soc. Am. Abstr. Programs*, *2*, 86.

Kay, R. W., and S. M. Kay (1993), Delamination and delamination magmatism, *Tectonophysics*, *219*, 177–189, doi:10.1016/0040-1951(93)90295-U.

Kennan, L., S. H. Lamb, and L. Hoke (Eds.) (1997), *High-Altitude Palaeosurfaces in the Bolivian Andes: Evidence for Late Cenozoic Surface Uplift*, *Geol. Soc. Spec. Publ.*, *120*, 307–323.

Koppers, A. A. P. (2002), ArArCALC: Software for $^{40}Ar/^{39}Ar$ age calculations, *Comput. Geosci.*, *28*, 605–619, doi:10.1016/S0098-3004(01)00095-4.

Lamb, S., and P. Davis (2003), Cenozoic climate change as a possible cause for the rise of the Andes, *Nature*, *425*, 792–797, doi:10.1038/nature02049.

Lamb, S., L. Hoke, L. Kennan, and J. Dewey (1997), Cenozoic evolution of the central Andes in Bolivia and northern Chile, in *Orogeny Through Time: An Overview*, edited by J.-P. Burg and M. Ford, *Geol. Soc. Spec. Publ.*, *121*, 237–264.

McGeary, S., A. Nur, and Z. Ben-Avraham (1985), Spatial gaps in arc volcanism: The effect of collision or subduction of oceanic plateaus, *Tectonophysics*, *119*, 195–221, doi:10.1016/0040-1951(85)90039-3.

Mégard, F. (1984), The Andean orogenic period and its major structures in central and northern Peru, *J. Geol. Soc. London*, *141*, 893–900, doi:10.1144/gsjgs.141.5.0893.

Miller, K. G., M. A. Kominz, J. V. Browning, J. D. Wright, G. S. Mountain, M. E. Katz, P. J. Sugarman, B. S. Cramer, N. Christie-Blick, and S. F. Pekar (2005), The Phanerozoic record of global sea-level change, *Science*, *310*(5752), 1293–1298, doi:10.1126/science.1116412.

Mortimer, C. (1973), The Cenozoic history of the southern Atacama Desert, Chile, *J. Geol. Soc. London*, *129*, 505–526, doi:10.1144/gsjgs.129.5.0505.

Muñoz, J. (1956), Chile, in *Handbook of South American Geology*, edited by W. F. Jenks, *Mem. Geol. Soc. Am.*, *65*, 187–241.

Muñoz, N., and R. Charrier (1996), Uplift of the western border of the Altiplano on a west-vergent thrust system, northern Chile, *J. South Am. Earth Sci.*, *9*(3–4), 171–181, doi:10.1016/0895-9811(96)00004-1.

Nester, P. L., T. E. Jordan, N. Blanco, G. D. Hoke, and A. J. Tomlinson (2006), Evidence for late Miocene uplift by long-wavelength rotation of western flank of Altiplano segment of central Andes 20°30′–20°30′S, Chile, *Geol. Soc. Am. Abstr. Programs*, *2*, 31.

Noble, D. C., E. H. McKee, and F. Mégard (1979), Early Tertiary "Incaic" tectonism, uplift, and volcanic activity, Andes of central Peru, *Geol. Soc. Am. Bull.*, *90*(10), 903–907, doi:10.1130/0016-7606(1979)90<903:ETITUA>2.0.CO;2.

Noble, D. C., E. H. McKee, T. Mourier, and F. Mégard (1990), Cenozoic stratigraphy, magmatic activity, compressive deformation, and uplift in northern Peru, *Geol. Soc. Am. Bull.*, *102*(8), 1105–1113, doi:10.1130/0016-7606(1990)102<1105:CSMACD>2.3.CO;2.

Nur, A., and Z. Ben-Avraham (1981), Volcanic gaps and the consumption of aseismic ridges in South America, *Mem. Geol. Soc. Am.*, *154*, 729–740.

Nur, A., and Z. Ben-Avraham (1983), Volcanic gaps due to oblique consumption of aseismic ridges, *Tectonophysics*, *99*, 355–362, doi:10.1016/0040-1951(83)90112-9.

Paola, C., and D. Mohrig (1996), Palaeohydraulics revisited: Palaeoslope estimation in coarse-grained braided rivers, *Basin Res.*, *8*, 243–254, doi:10.1046/j.1365-2117.1996.00253.x.

Pardo-Casas, F., and P. Molnar (1987), Relative motion of the Nazca (Farallon) and South American plates since Late Cretaceous time, *Tectonics*, *6*(3), 233–248, doi:10.1029/TC006i003p00233.

Pecho, G. (1983), Mapa geológico del cuadrángle de Caravelí, scale 1:100,000, Inst. Geol. Minero y Metal., Lima.

Pilger, R. H., Jr. (1981), Plate reconstructions, aseismic ridges, and low-angle subduction beneath the Andes, *Geol. Soc. Am. Bull.*, *92*(7), 448–456, doi:10.1130/0016-7606(1981)92<448:PRARAL>2.0.CO;2.

Pinto, L., G. Herail, and R. Charrier (2004), Sedimentación sintectónica asociada a las estructuras néogenas en la Precordillera de la zona de Moquella, Tarapacá (19°15′S, norte de Chile), *Rev. Geol. Chile*, *31*, 19–44.

Quade, J., C. Garzione, and J. Eiler (2007), Paleoelevation reconstruction using pedogenic carbonates, *Rev. Mineral. Geochem.*, *66*, 53–87.

Ramos, V. A., E. O. Cristallini, and D. J. Perez (2002), The pampean flat-slab of the central Andes, *J. South Am. Earth Sci.*, *15*(1), 59–78, doi:10.1016/S0895-9811(02)00006-8.

Ranero, C. R., and R. von Huene (2000), Subduction erosion along the Middle America convergent margin, *Nature*, *404*, 748–752, doi:10.1038/35008046.

Reiners, P. W. (2005), Zircon (U-Th)/He thermochronometry, in *Low-Temperature Thermochronology: Techniques, Interpretations, and Applications*, *Rev. Mineral. Geochem.*, vol. 58, edited by P. W. Reiners and T. A. Ehlers, pp. 151–179, Mineral. Soc. of Am., Washington, D. C.

Reiners, P. W., K. A. Farley, and H. J. Hickes (2002), He diffusion and (U-Th)/He thermochronometry of zircon: Initial results from Fish Canyon Tuff and Gold Butte, *Tectonophysics*, *349*, 297–308, doi:10.1016/S0040-1951(02)00058-6.

Renne, P. R., C. C. Swisher, A. L. Deino, D. B. Karner, T. L. Owens, and D. J. DePaolo (1998), Intercalibration of standards, absolute ages and uncertainties in $^{40}Ar/^{39}Ar$ dating, *Chem. Geol.*, *145*, 117–152, doi:10.1016/S0009-2541(97)00159-9.

Roperch, P., T. Sempere, O. Macedo, C. Arriagada, M. Fornari, C. Tapia, M. García, and C. Laj (2006), Counterclockwise rotation of late Eocene–Oligocene fore-arc deposits in southern Peru and its significance for oroclinal bending in the central Andes, *Tectonics*, *25*, TC3010, doi:10.1029/2005TC001882.

Sáez, A., L. Cabrera, A. Jensen, and G. Chong (1999), Late Neogene lacustrine record and palaeogeography in the Quillagua-Llamara basin, central Andean fore-arc (northern Chile), *Palaeogeogr. Palaeoclimatol. Palaeoecol.*, *151*, 5–37, doi:10.1016/S0031-0182(99)00013-9.

Schildgen, T. F., K. V. Hodges, K. X. Whipple, P. W. Reiners, and M. S. Pringle (2007), Uplift of the western margin of the Andean plateau revealed from canyon incision history, southern Peru, *Geology*, *35*(6), 523–526, doi:10.1130/G23532A.1.

Schildgen, T. F., T. Ehlers, M. van Soest, D. Whipp, K. X. Whipple, and K. V. Hodges (2008), Quantifying canyon incision and Andean Plateau surface uplift, southwest Peru: A thermochronometer and numerical modeling approach, *Geophys. Res. Abstr.*, *10*, EGU2008-A-08016, sref:1607-7962/gra/EGU2008-A-08016.

Sébrier, M., and P. Soler (1991), Tectonics and magmatism in the Peruvian Andes from late Oligocene time to the present, in *Andean Magmatism and Its Tectonic Setting*, edited by R. S. Harmon and C. W. Rapela, *Spec. Pap. Geol. Soc. Am.*, *265*, 259–278.

Sébrier, M., J. L. Mercier, F. Mégard, G. Laubacher, and E. Carey-Gailhardis (1985), Quaternary normal and reverse faulting and the state of stress in the central Andes of south Peru, *Tectonics*, *4*(7), 739–780, doi:10.1029/TC004i007p00739.

Singewald, J. T., Jr., and E. W. Berry (1922), *The Geology of the Corocoro Copper District of Bolivia*, *Johns Hopkins Univ. Stud. Geol.*, *1*, 117 pp.

Somoza, R. (1998), Updated Nazca (Farallon)—South America relative motions during the last 40 My: Implications for mountain building in the central Andean region, *J. South Am. Earth Sci.*, *11*(3), 211–215, doi:10.1016/S0895-9811(98)00012-1.

Spotila, J. A., K. A. Farley, and K. Sieh (1998), Uplift and erosion of the San Bernardino Mountains associated with transpression along the San Andreas fault, California, as constrained by radiogenic helium thermochronometry, *Tectonics*, *17*(3), 360–378, doi:10.1029/98TC00378.

Steiger, R. H., and E. Jäger (1977), Subcommission on geochronology: Convention on the use of decay constants in geo- and cosmochronology, *Earth Planet. Sci. Lett.*, *36*, 359–362, doi:10.1016/0012-821X(77)90060-7.

Steinmann, G. (1929), *Geologie von Peru*, 448 pp., Heidelberg Univ., Heidelberg, Germany.

Thouret, J.-C., G. Wörner, Y. Gunnell, B. Singer, X. Zhang, and T. Souriot (2007), Geochronologic and stratigraphic constraints on canyon incision and Miocene uplift of the central Andes in Peru, *Earth Planet. Sci. Lett.*, *263*, 151–166, doi:10.1016/j.epsl.2007.07.023.

Tosdal, R. M., A. H. Clark, and E. Farrar (1984), Cenozoic polyphase landscape and tectonic evolution of the Cordillera Occidental, southernmost Peru, *Geol. Soc. Am. Bull.*, *95*(11), 1318–1332, doi:10.1130/0016-7606(1984)95<1318:CPLATE>2.0.CO;2.

Victor, P., O. Oncken, and J. Glodny (2004), Uplift of the western Altiplano plateau: Evidence from the Precordillera between 20° and 21°S (northern Chile), *Tectonics*, *23*, TC4004, doi:10.1029/2003TC001519.

von Huene, R., and C. R. Ranero (2003), Subduction erosion and basal friction along the sediment-starved convergent margin off Antofagasta, Chile, *J. Geophys. Res.*, *108*(B2), 2079, doi:10.1029/2001JB001569.

Wörner, G., D. Uhlig, I. Kohler, and H. Seyfried (2002), Evolution of the West Andean Escarpment at 18°S (N. Chile) during the last 25 Ma: Uplift, erosion and collapse through time, *Tectonophysics*, *345*, 183–198, doi:10.1016/S0040-1951(01)00212-8.

York, D. (1968), Least squares fitting of a straight line with correlated errors, *Earth Planet. Sci. Lett.*, *5*, 320–324, doi:10.1016/S0012-821X(68)80059-7.

K. Cornell and M. S. Pringle, Department of Earth, Atmospheric and Planetary Sciences, Massachusetts Institute of Technology, Cambridge, MA 02139, USA.

K. V. Hodges, M. van Soest, and K. X. Whipple, School of Earth and Space Exploration, Arizona State University, Tempe, AZ 85287, USA.

T. F. Schildgen, Department of Geosciences, University of Potsdam, Potsdam D-14476, Germany. (tschild@uni-potsdam.de)